

The 30 November 2018 M_w 7.1 Anchorage Earthquake

by Michael E. West, Adrian Bender, Matthew Gardine, Lea Gardine, Kara Gately, Peter Haeussler, Wael Hassan, Franz Meyer, Cole Richards, Natalia Ruppert, Carl Tape, John Thornley, and Rob Witter

ABSTRACT

The M_w 7.1 47 km deep earthquake that occurred on 30 November 2018 had deep societal impacts across southcentral Alaska exhibited phenomena of broad scientific interest. We document observations that point to future directions of research and hazard mitigation. The rupture mechanism, aftershocks, and deformation of the mainshock are consistent with extension inside the Pacific plate near the down-dip limit of flat-slab subduction. Peak ground motions $>25\%g$ were observed across more than 8000 km², though the most violent near-fault shaking was avoided because the hypocenter was nearly 50 km below the surface. The ground motions show substantial variation, highlighting the influence of regional geology and near-surface soil conditions. Aftershock activity was vigorous with roughly 300 felt events in the first six months, including two dozen aftershocks exceeding M 4.5. Broad subsidence of up to 5 cm across the region is consistent with the rupture mechanism. The passage of seismic waves and possibly the coseismic subsidence mobilized ground waters, resulting in temporary increases in stream flow. Although there were many failures of natural slopes and soils, the shaking was insufficient to reactivate many of the failures observed during the 1964 M 9.2 earthquake. This is explained by the much shorter duration of shaking as well as the lower amplitude long-period motions in 2018. The majority of observed soil failures were in anthropogenically placed fill soils. Structural damage is attributed to both the failure of these emplaced soils as well as to the ground motion, which shows some spatial correlation to damage. However, the paucity of instrumental ground-motion recordings outside of downtown Anchorage makes these comparisons challenging. The earthquake demonstrated the challenge of issuing tsunami warnings in complex coastal geographies and highlights the need for a targeted tsunami hazard evaluation of the region. The event also demonstrates the challenge of estimating the probabilistic hazard posed by intraslab earthquakes.

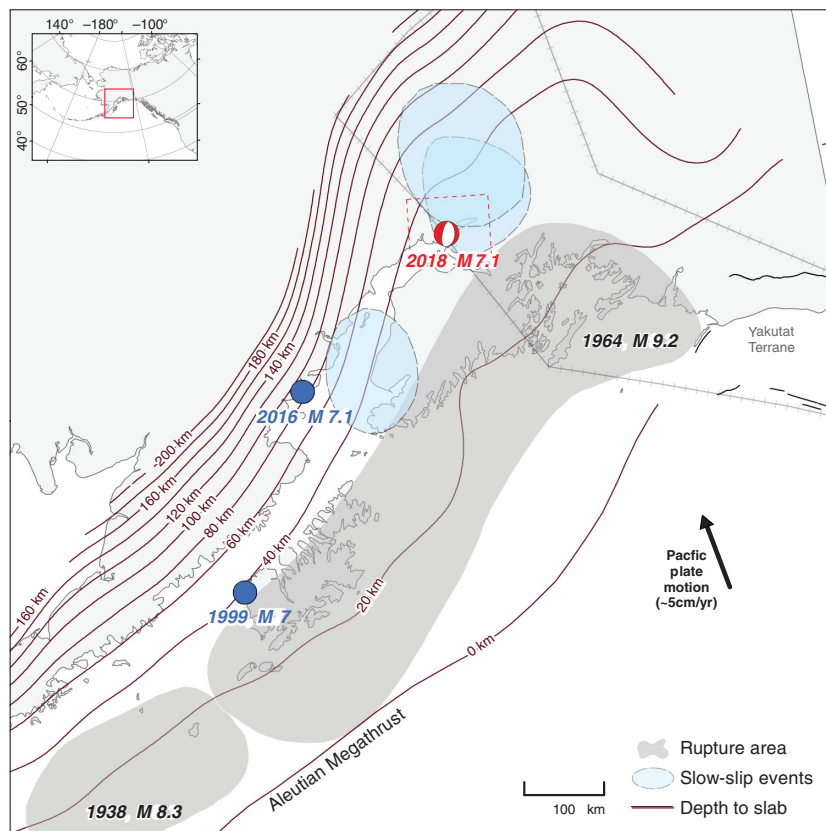
Supplemental Material

INTRODUCTION

On the morning of 30 November 2018, southcentral Alaska experienced the most societally significant earthquake in the region in half a century. The M_w 7.1 earthquake occurred nearly 50 km beneath Anchorage inside the subducting slab as a result of tensional forces near the transition from flat to steeply dipping slab. Strong to severe shaking was felt by more than half of Alaska's population. Because the earthquake impacted so many sectors of society, it is arguably the best earthquake learning experience in Alaska since the M_w 9.2 Great Alaska earthquake in 1964. The purpose of this article is to provide an introduction to the observations and impacts across disciplines.

Anchorage and southcentral Alaska experience frequent shaking from earthquakes occurring on the Alaska–Aleutian subduction zone interface. But earthquakes inside the subducting slab and in the overlying crust add to the hazard. Magnitude 4 and 5 earthquakes are felt routinely, albeit lightly, by the majority of Alaskans. Even large earthquakes occur with some regularity. More than 80% of the M 6+ earthquakes in the United States occur in Alaska and surrounding waters. Averaged over decades, M 7+ earthquakes occur somewhere along the arc every other year, though the past few years have exceeded this rate.

From this perspective, the M_w 7.1 earthquake was not exceptional and did not surprise anyone familiar with the region's tectonics. What made this earthquake unusual was its proximity to human population. The population of Alaska is small compared with other parts of the United States and is clustered in a handful of locations separated by hundreds of kilometers. Hence, the vast majority of earthquakes occur at considerable distance from human population. The earthquake ground motions felt routinely are nearly always low-frequency rumbles from distant earthquakes or the abrupt modest tremors of small local earthquakes. Even larger recent earthquakes, such as the 2002 M_w 7.9 Denali fault earthquake (Eberhart-Phillips *et al.*, 2003), the 2013 M_w 7.5 Craig earthquake (Yue *et al.*, 2013), the 2014 M_w 7.9 Little Sitkin earthquake (Macpherson and Ruppert, 2015), and the January 2018 M_w 7.9 Offshore Kodiak earthquake (Ruppert *et al.*,



▲ **Figure 1.** Regional setting. Contours mark depth to slab. Significant subduction zone earthquake rupture patches are marked in gray. Slow-slip events (light blue) from Fu and Freymueller (2013) and references therein. Inferred Yakutat terrane from Eberhardt-Phillips *et al.* (2006). See E Text S1 for moment tensor details. The red box in the inset marks the location of Southcentral Alaska.

2018), had only minor impacts. In each case, the impact of these earthquakes was tempered by distance from human population and the absence of significant tsunamis.

The most notable exception for Anchorage is the 1964 M_w 9.2 Great Alaska earthquake. The 700 km long rupture generated violent ground motions across southern Alaska and generated a tsunami with fatal impacts from Alaska to California. Although the majority of damage and fatalities resulted from the tsunami (Lander, 1996), which did not extend to Anchorage, the damage from strong ground motion was extensive (Hansen, 1965). The shaking caused widespread damage to buildings and infrastructure that had been constructed with limited regard for seismic resilience. The most significant failures were not caused by the amplitude of the shaking. Instead, the ground motions, which lasted many minutes and were rich in long-period energy, triggered widespread ground failures (Hansen, 1965). The repeated strain cycling of wet unconsolidated soils (i.e., loosely arranged, lacking strong bonds) and clays caused slumping, landslides, liquefaction, and in some more notorious cases the complete sloughing of steep bluffs.

The reconstruction in the decade following the 1964 earthquake coincided with a boom in Alaska development tied to the discovery of oil. The rapid growth and optimism about the future

—buoyed by statehood in 1958—led the state, and Anchorage in particular, to adopt a proactive stance toward safe development. With the memories of 1964 still raw, Anchorage adopted notably progressive building codes for the time. Even the state legislature wrote explicit seismic requirements into many of its laws.

Anchorage today is a product of this history. The municipality of Anchorage is home to 300,000 of the state's 740,000 residents. The greater Anchorage region, including the Matanuska–Susitna (Mat-Su) valley, adds another 100,000. Anchorage infrastructure, especially in its outlying areas, is generally young. The population of Anchorage has grown more than threefold since 1964. Although a portion of the infrastructure predates the worldwide introduction of seismic construction details in the early 1980s, much of the development boom occurred after the introduction of these standards. Oversight and code enforcement vary by location but are good in downtown Anchorage. Taken together, these various factors have led to a city that has made an honest effort at seismic resilience.

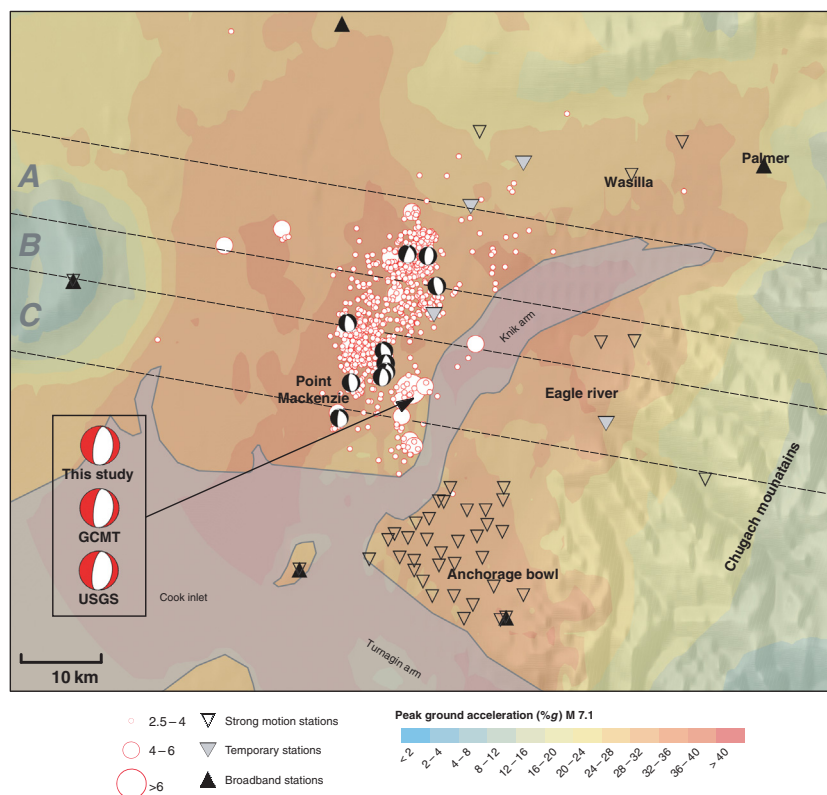
The 30 November earthquake represents the first critical test of these efforts. There has been no magnitude 6 or larger earthquakes within 100 km of Anchorage in the past half a century. In 2012, an M 5.8 earthquake 30 km north–northwest of Anchorage generated ground motions of $\sim 5\%$ g in the downtown area, and an M 6.4 in 1983 caused damage to a school that had previously been flagged for poor construction. In 2016,

the M_w 7.1 Iniskin earthquake produced ground motions in the 10%–15%g range (Grapenthin *et al.*, 2018). Isolated cases of damage were recorded, primarily from secondary influences such as ruptured natural gas lines. However, the earthquake occurred 250 km away from Anchorage, and the damage was light enough so that no systematic effort was undertaken to compile and assess damages. The Iniskin earthquake highlighted the urban hazard potential of earthquakes generated inside the subducting Pacific plate and the possible effects of nearby sedimentary basins.

Although the Anchorage earthquake was far from a worst-case scenario, its impact was profound. It tested the region's earthquake preparedness and shortcomings more than any earthquake in recent history. This makes it a rare learning experience. Many of these topics will be examined in detail by later studies. By providing a broad multidisciplinary overview, the authors hope to catalyze subsequent research that is both insightful and societally relevant.

TECTONIC SETTING AND EARTHQUAKE SOURCE

This earthquake occurred at the northeastern end of the Alaska–Aleutian subduction zone, where the subducting Pacific plate is moving to the north–northwest at about



▲ **Figure 2.** Mainshock epicenter with regional peak ground acceleration (PGA) contours. Aftershock locations are shown in red. Strong motion and broadband seismic stations locations are keyed to the legend. Boxes mark cross sections shown in Figure 3.

5.1 cm/yr (Fig. 1). The tectonics of the region include the collision and subduction of the Yakutat terrane, which has characteristics of an oceanic plateau (Christeson *et al.*, 2010). The subduction zone has a very shallow dip, which is attributed to the high buoyancy and thickness of the subducted Yakutat slab compared with a typical oceanic slab (Ferris *et al.*, 2003; Eberhart-Phillips *et al.*, 2006; Abers, 2008; Haeussler, 2008). Seismicity follows the slab to a depth of about 200 km, below which the slab appears to descend steeply to at least 400 km depth (Burdick *et al.*, 2017; Jiang *et al.*, 2018; Martin-Short *et al.*, 2018). The 47 km depth of the mainshock is consistent with being in the upper part of the subducting slab (see Kim *et al.*, 2014). Because the earthquake is near the point where the slab begins to pull away from the overlying crust, it is unclear whether the slab is overlain by warm mantle material or cold forearc crust.

The mainshock was followed five minutes later by an M_w 5.7 aftershock—the largest aftershock to date. During the first two months, there were more than 8000 aftershocks with a magnitude of completeness of 1.5 and b -value of 0.77 (Okal and Romanowicz, 1994). Roughly 40 of these aftershocks exceeded M 4. Compared with other nearby intraslab earthquakes, such as the 1999 M_w 7.0 Kodiak and the 2016 M_w 7.1 Iniskin events (Fig. 1), this aftershock sequence produced significantly more M 3–5 aftershocks, leading to its relatively low b -value. Although large aftershocks (M 4+) were

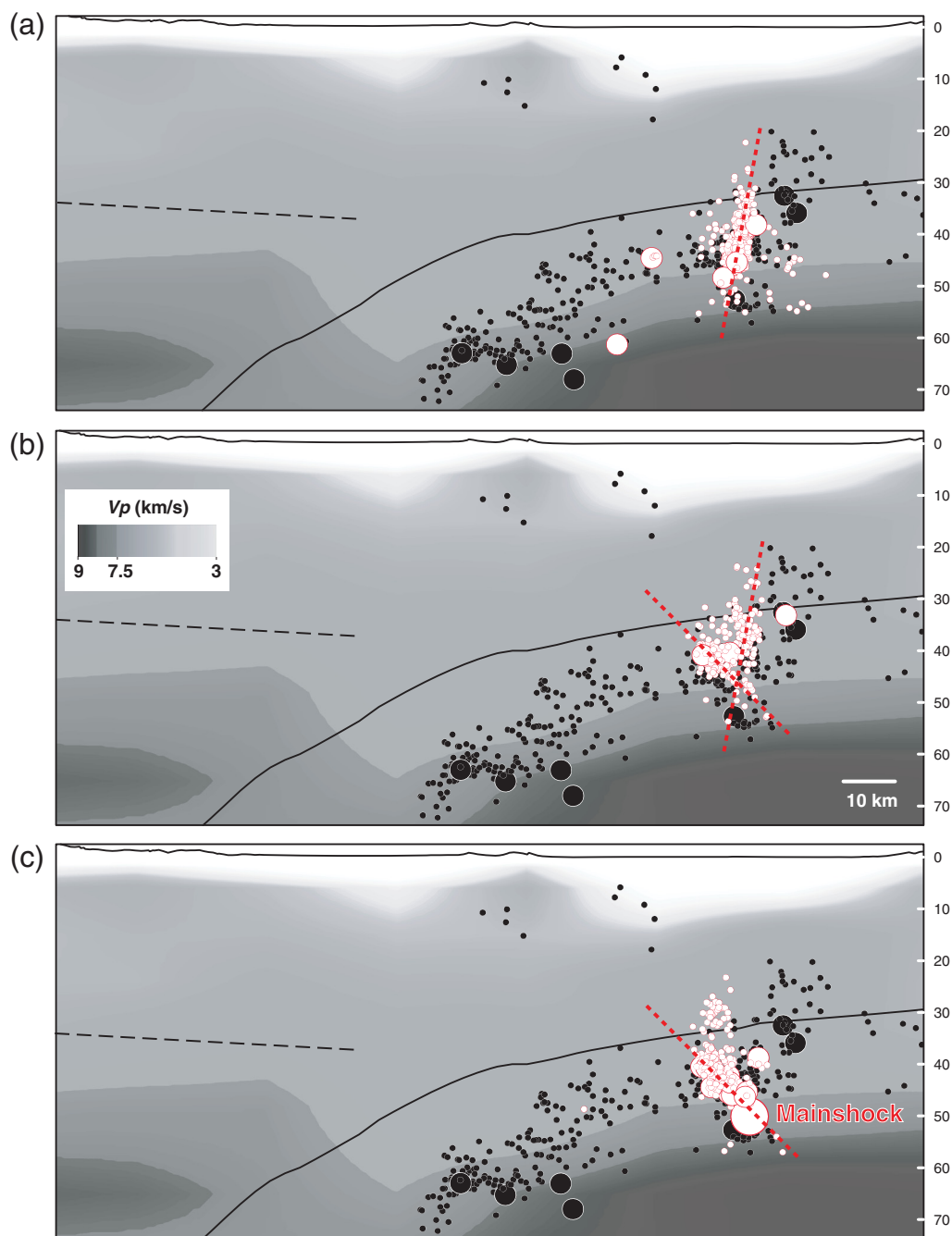
distributed throughout the aftershock zone at the beginning of the sequence, later M 4+ aftershocks occurred farther away from the mainshock rupture.

There is a good focal mechanism agreement for the mainshock between the Global Centroid Moment Tensor project solution and the U.S. Geological Survey (USGS) (both shown in Fig. 2). The mechanism is consistent with the persistent historical normal faulting observed by Ruppert (2008). Liu *et al.* (2019) present multiple finite-fault solutions assuming motion on each of the two nodal planes. They find a slightly better fit to waveform and Global Positioning System data on the west-dipping plane, though the results are not conclusive. Kinematic models from Liu *et al.* (2019) are in good agreement with a rupture that lasted about 12 s, propagated to the north, and expanded both deeper and shallower for a total vertical extent of around 20 km.

We relocate aftershocks to better determine the geometric distribution of the rupture. We use the double-difference algorithm of Waldhauser and Ellsworth (2000) to relocate 894 $M \geq 2.5$ aftershocks as well as 610 $M \geq 2.5$ earthquakes that occurred during the prior 10 yr. We include phase picks from permanent broadband and strong-motion stations as well as picks from temporary stations installed a week after the earthquake (Fig. 2).

The relocated aftershocks extend ~ 25 km northward along a strike that agrees well with the strike of the mainshock. Aftershock depths range from 22 to 61 km, with 95% of the events between 31 and 48 km, consistently shallower than the mainshock. The relocated aftershocks form at least two distinct clusters. The northern cluster is offset slightly to the east of the southern cluster. Relocated hypocenters also hint at a different fault plane for each cluster. In the northern part of the aftershock zone, the fault plane appears to dip quite steeply ($\sim 80^\circ$) to the west (Fig. 3). In the southern cluster, the aftershock lineation dips more shallowly to the east ($\sim 45^\circ$).

We use long-period regional seismic waveforms to estimate focal mechanisms (Zhu and Helmberger, 1996; Silwal and Tape, 2016) for 10 well-distributed aftershocks of M_w 4.5–5.0 (see © Text S1, available in the supplemental material to this article). The resulting focal mechanisms are remarkably similar to no systematic evolution with time or location (Fig. 2). The two fault planes implied by the mainshock and aftershock mechanisms strike essentially north-south and dip either east 30° or west 60° . These dips agree qualitatively with the planes suggested by aftershocks, though they do not align exactly. It is possible that errors in the local velocity model are stretching the true aftershock depths into a more vertical profile, which erroneously steepens both the east- and west-dipping planes.



▲ **Figure 3.** Cross sections through the cloud of aftershocks (white). Historical seismicity is shown in black. Larger circles are $M \geq 4$. Gray contours are from the P -wave tomographic model of Eberhart-Phillips *et al.* (2019). Solid black line marks the plate interface of Slab2 (Hayes *et al.*, 2018). Dashed black lines marks inferred continental Moho after Miller *et al.* (2018). (a–c) Aftershocks correspond to the three cross-section boxes outlined in Figure 2. See Figure 2 legend for aftershock size scaling.

The mainshock rupture can be characterized by reconciling the aftershock distribution, finite-source models, and point-source models for both the mainshock and aftershocks. One possibility is that the mainshock initiated in the south on an east-dipping plane then migrated northward to the west-dipping plane. In this scenario, both portions of the rupture would be roughly consistent with the mainshock focal mechanism (as the sum of slip on two very different faults) and the

aftershock focal mechanisms. This would also imply that—despite notable similarity among the aftershock focal mechanisms—the events in the north are rupturing along the steep west-dipping plane, whereas the events in the south are rupturing along the east-dipping plane. In this model, the two distinct pulses of seismic moment release in the source time function of Liu *et al.* (2019) might reflect rupture on two different faults.

A second possibility is that the mainshock ruptured one of the two planes and then triggered aftershocks on a separate plane that happened to be similarly oriented to the auxiliary plane of the mainshock rupture. There are prior examples of intraslab earthquakes stimulating aftershocks on adjacent faults (e.g., Macpherson and Ruppert, 2015; Melgar, Ruiz-Angulo, *et al.*, 2018). As with the first possibility, this model would suggest that the fault plane of the larger aftershocks essentially flips between the north and south clusters.

A third possibility is that one fault plane was responsible for the mainshock and aftershocks. This was the assumption used within the finite-source modeling of Liu *et al.* (2019), who showed (their fig. 5) that the preliminary aftershock locations did not align with either of the two fault planes of the mainshock mechanism. The one-fault interpretation would imply that the complex aftershock patterns in Figure 3 are either incorrect (perhaps distorted by the influence of strong heterogeneity) or are unrelated to the geometry of the rupture of the mainshock. This possibility seems to be the least likely among the three.

Future studies that include higher precision aftershock relocations, 3D seismic velocities, and multipane finite-source models should be able to validate or rule out the various models mentioned earlier.

TSUNAMI ASSESSMENT

The National Tsunami Warning Center (NTWC) issues tsunami alerts for the coasts of Canada and the continental United States (Department of Commerce, National Oceanic & Atmospheric Administration, National Weather Service, 2009) with localized warnings for the U.S. Pacific coastline beginning at M 7.1 (Whitmore *et al.*, 2008). For earthquakes with sources near the U.S. coastline, tsunami bulletins are issued within 5 min of origin time. To provide the earliest alerts possible, initial warnings are based on earthquake location and magnitude.

Three to four minutes after the 30 November earthquake, initial magnitude estimates showed good agreement of M_{wp} 6.8–7.0, leading NTWC to issue a tsunami information statement. Roughly five minutes after the earthquake, Earlybird software began providing magnitudes of M_{wp} 7.2–7.4 (Huang *et al.*, 2007). Following special procedures for interior waterways which begin at $M \geq 7.1$ (Whitmore *et al.*, 2008), NTWC issued a tsunami warning for the coastlines of Cook Inlet and the southern Kenai Peninsula, with a preliminary magnitude of M_{wp} 7.2 (© Fig. S1). (see [Data and Resources](#))

Protocol is to hold an initial tsunami alert until it can be confirmed that there is no danger. At 25 min past origin time, the Pacific Tsunami Warning Center provided NTWC with a W-phase magnitude (Wang *et al.*, 2017) of M_w 7.17 (© Table S1). This was followed at 29 min after origin time by an M_{ww} 7.0 solution, with a normal-faulting mechanism, from the National Earthquake Information Center (NEIC). NTWC protocol is to issue products following NEIC's

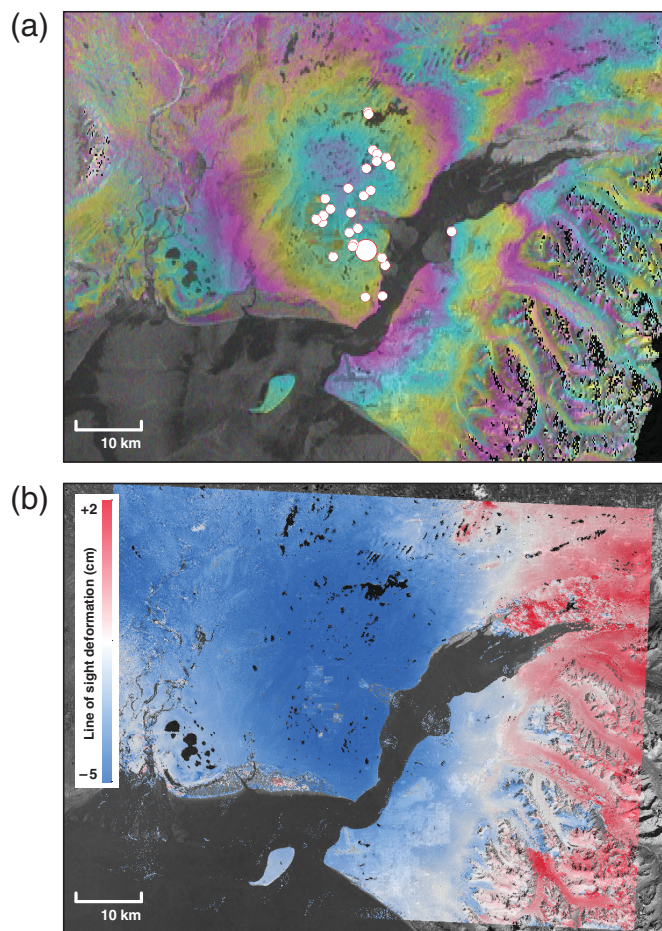
information when it is released. NTWC revised the magnitude to M 7.0 on tsunami warning number 2 (issued 30 min after origin time) and continued to assess the coastal hazard, considering all possible tsunami sources and locations. The immediate concerns focused on the potential for coastal liquefaction and ground failure (especially near the Little Susitna river and Susitna river deltas, and Ship Creek), underwater slumping in Cook Inlet, and landslides in Turnagain Arm. From the ShakeMap (Fig. 2), NTWC was able to determine that the rupture was largely to the north of the epicenter and not under Cook Inlet. This alleviated some concerns for underwater slumping. The new USGS ground failure and liquefaction estimates were also helpful in this regard (© Fig. S2), although the absence of bathymetry and underwater hazards currently limit their use for tsunami applications.

Several factors combine to reduce tsunami impacts in upper Cook Inlet. The water depth does not generally exceed 20 m, and Anchorage is surrounded by extensive tidal flats. The tide at the time of the earthquake was also low. However, there has been no comprehensive study of tsunami hazard in upper Cook Inlet. The 1964 earthquake demonstrated that the bluffs and mudflats characteristic of the area are prone to sliding under the right conditions. It is unclear, however, how tsunamigenic these modes of failure may or may not be. Although the tsunamigenic potential of these slides is uncertain, similar geology in the Puget sound region has been known to generate impactful tsunamis (González *et al.*, 2003).

The tide gauge at the Port of Anchorage confirmed that no massive slumping or ground failures occurred in the Anchorage area. The remaining tide gauges, in Nikiski and Seldovia, were too far from the source to be useful in rapid assessment. Shallow-water travel-time estimates from likely sources within Cook Inlet to the Anchorage tide gauge were used to determine how long to wait before issuing an all clear. Because tsunami travel times are much slower in the shallow waters of Cook Inlet, substantial time was needed before declaring an all clear. Because of the large amount of unmonitored and unpopulated coastline, NTWC also queried numerous partners for reports of coastal waves or unusual water activity before cancelling the tsunami warning 90 min after origin time (© Table S1).

DEFORMATION

Interferometric Synthetic Aperture Radar (InSAR) provides a broad view of deformation caused by the earthquake. Despite the long-demonstrated ability of Synthetic Aperture Radar (SAR) to map coseismic deformation (e.g., Wright *et al.*, 2003; Lu *et al.*, 2003), it was not until the recently launched Sentinel-1 C-band SAR constellation, with its regularly acquired and free-and-open data, that SAR has been elevated to a widespread data source for routine hazards monitoring and response (Potin *et al.*, 2014; Meyer *et al.*, 2015; Ajadi *et al.*, 2016). One approach to this is the SARVIEWS processing system (see [Data and Resources](#)), a fully automated monitoring service providing rapid image and deformation information



▲ **Figure 4.** SARVIEWS Sentinel-1 interferometry. (a) Interferogram showing the cumulative surface deformation between the 12-day period 22 November to 4 December 2018. M_w 4+ aftershocks between 30 November and 4 December shown as white circles. Larger circle is the mainshock. One cycle of color contours corresponds to 2.8 cm of deformation in the line of sight of the satellite. Stippled data indicates areas of low-signal coherence. (b) Line of sight surface deformation derived from the interferogram. The image aggregates all motion during this time including the mainshock and aftershocks.

from Sentinel-1 SAR for events related to severe weather, earthquakes, and volcanic unrest. (See © Text S2 for a detailed overview of SARVIEWS processing.)

Following the Anchorage earthquake, the first postevent Sentinel-1 acquisitions (descending orbit direction) became available 4 December at 16:18 UTC, five days after the event. The Sentinel-1 observation strategy over the Anchorage area favored descending orbit geometries at the time of the event, so an earlier acquisition opportunity on 1 December (ascending orbit direction) was not realized.

The SARVIEWS processing protocol (© Text S2) is to pair the postevent image with the two prior InSAR images closest in time. Interferograms were formed with acquisitions from 10 to 22 November 2018, resulting in 12- and 24-day interferograms. Weather conditions before and after the

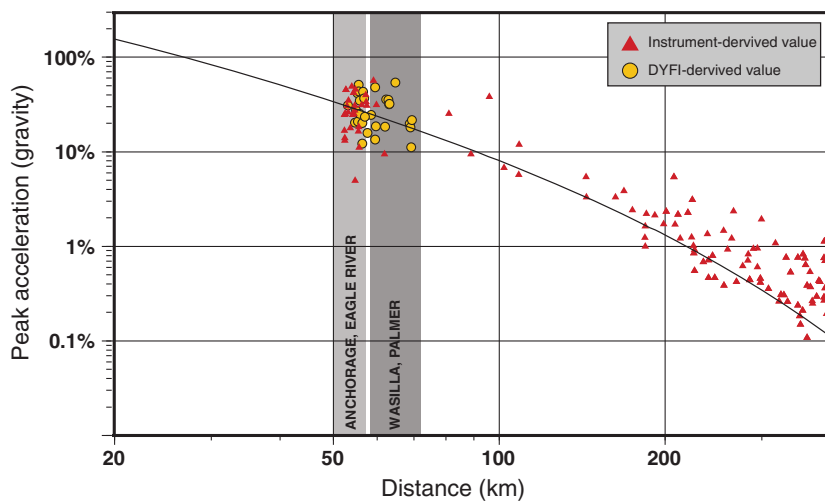
earthquake were not conducive to strong InSAR coherence, with temperatures fluctuating around freezing and a mix of snow and rain. The 24-day interferogram (not shown) lacked sufficient coherence. The 12-day interferogram, however, reveals clear systematic patterns centered on the epicenter (Fig. 4a).

The repeating cycles of phase information in Figure 4a can be compounded, or unwrapped, and scaled to surface deformation in the line of sight direction of the satellite (Fig. 4b). Although the line of sight vector includes both a vertical and horizontal component, based on the source depth and mechanism, we infer that this displacement field largely reflects vertical motion. The unwrapped data demonstrate that whereas areas northwest of the epicenter moved downward by more than 5 cm, comparatively modest uplift was recorded toward the east. Although Figure 4b aggregates all deformation between 22 November and 4 December, the aftershocks have far smaller moment release and are presumably negligible contributions compared with the mainshock. The predominant downward deformation across the region is consistent with the normal-fault focal mechanism of the mainshock and extension in the slab. The uplift to the east of the source region, which is not observed immediately to the west of the source region, favors the steep west-dipping fault plane over the east dipping, broadly consistent with observations in the [Tectonic Setting and Earthquake Source](#) section.

GROUND MOTION

Ground motion from this earthquake was sufficient to saturate broadband sensors within a few hundred kilometers of the epicenter, rendering them unusable for estimates of shaking. Fortunately, the area has better strong-motion capabilities than most of Alaska (Fig. 2). Strong-motion instruments provided high-fidelity acceleration records at dozens of locations in the densely populated Anchorage Bowl—the low-lying peninsular region that includes the most developed areas of the city. At more distant sites that lack strong-motion capabilities, broadband velocities were derived to create acceleration records. These are used together with the empirical relationships of [Worden *et al.* \(2012\)](#) to provide a ground intensity measure in the ShakeMap. When no ground-motion records exist, shaking can be estimated from ground-motion prediction equations (GMPEs). Together these two data types provided the underpinnings of the various ShakeMaps for the event. At the time of the earthquake, the Alaska Earthquake Center was using the USGS ShakeMap version 3.0 (v.3.0) software to produce ShakeMap parameters and geospatial data served through the center's website and through the Advanced National Seismic System (ANSS) ComCat portal (see [Data and Resources](#)).

Although the initial ShakeMaps were based on automated processing, later iterations were manually curated to incorporate as many additional observations as possible, from partners including USGS, the Incorporated Research Institutions for Seismology (IRIS) Transportable Array, the NTWC, and the Alaska Volcano Observatory. Key among



▲ **Figure 5.** Instrumental and inferred PGAs as a function of 3D distance from the source. Black line marks the estimate from the [Zhao *et al.* \(2006\)](#) ground-motion prediction equation (GMPE) used to derive the ShakeMap for this earthquake.

these data are the dense observations in and around downtown Anchorage provided by the dedicated urban strong-motion network ([Martirosyan *et al.*, 2002](#); [Dutta *et al.*, 2009](#)). Although these observations provide excellent coverage in the Anchorage Bowl, strong-motion data are sparse or absent in other population centers, including Wasilla, Palmer, and Eagle river. To account for the lack of instrumental data, the Alaska Earthquake Center decided to include aggregated “Did You Feel It?” (DYFI) reports from the USGS. Although these data are inherently qualitative, they have been shown to correlate with certain aspects of instrumental recordings ([Caprio *et al.*, 2015](#)). The ShakeMaps were further enhanced by including a 20 km long north-northeast-striking linear source inferred from aftershocks and estimates of finite-fault motion. When combined, these various data sets provide the best-available assessment of shaking patterns across southcentral Alaska.

The shaking pattern is best described as a broad region of moderate to strong ground motion. While the highest peak ground accelerations (PGAs) exceed 50%g, accelerations of 25%g or more were experienced across an area of more than 8000 km². Because of the earthquake’s depth, no person, building, or infrastructure was within 50 km of the hypocenter (© Fig. S4). The earthquake depth is singularly responsible for the absence of stronger ground motions that would have been expected for a shallow earthquake of comparable magnitude (e.g., [Boore *et al.*, 2014](#)). The depth is also responsible for the broadly uniform distribution of shaking over a large area. The true hypocentral distance varies much less than a map view perspective of the epicenter suggests.

Figure 5 shows the estimated PGA values as a function of hypocentral distance using the [Zhao *et al.* \(2006\)](#) GMPE that underlies the ground acceleration estimates in Figure 2. Superimposed are the instrumentally recorded PGA values (triangles), as well as the PGA values inferred from DYFI reports. The distribution illustrates PGA exceeding 10%g at 100 km

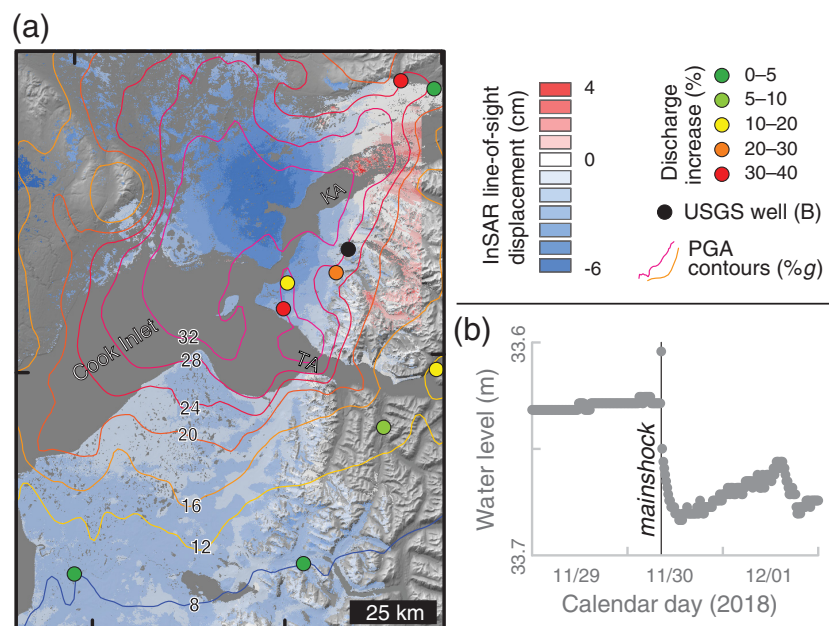
from the source, reinforcing the broad extent of strong ground motions. Beyond ~100 km, the measured accelerations progressively exceeded the GMPE-predicted values. Site class adjustments or a regionally tuned GMPE would likely bring this into better alignment.

The length scale of the ShakeMap reflects the sparse distribution of instrumental records. Figure 5 demonstrates that the ground motion varied over short distances in ways that are not captured in the ShakeMap. The only V_{S30} corrections used are the theoretical adjustments of [Wald and Allen \(2007\)](#) inferred from topography—no empirical V_{S30} data layer available across the region. Downtown Anchorage is the only area with sufficient observations to constrain shorter length-scale variations in the ground motion. The scatter in Figure 5 demonstrates shortcomings in our knowledge of site effects across the region. This is a clear direction for research and one that can directly impact seismic hazard assessments going forward.

HYDROLOGIC RESPONSE

Within minutes of the earthquake, hydrologic sensors in the region registered water level changes that persisted for days to weeks. By noon of the following day, nine ice-free stream gauges recorded increases of 2%–40% (Fig. 6a). In addition, groundwater levels in the only monitored well decreased by ~6 cm (Fig. 6b). Researchers attribute similar observations from other earthquakes to increases in aquifer permeability and pore pressure caused by static stress changes and/or dynamic strain from passing seismic waves ([Manga and Wang, 2015](#), and references therein). Several lines of evidence suggest that the hydrologic response was caused by the expulsion of groundwater: (1) the increases in discharge scale with the discharge prior to the earthquake, which should reflect the size of the shallow aquifer systems feeding each river under frozen surface conditions (© Fig. S5a); (2) increased streamflow was accompanied by temperature increases of 1°–2°C (see [Data and Resources](#)) suggesting water from the subsurface where ambient temperatures are comparatively warmer at that time of year; and (3) a drop in water level is observed in the sole monitored well (Fig. 6b). None of the gauges are located near the epicenter, and the discharge occurred in regions where liquefaction was neither observed at the surface (see the [Failure of Natural Materials](#) section) nor predicted (© Fig. S2). The rapid hydrologic response, however, suggests that subsurface liquefaction may have contributed to the increase in flow ([Manga, 2001](#); [Montgomery and Manga, 2003](#)).

To examine whether these observations could result from permanent changes in strain, we use the InSAR-derived subsidence (Fig. 4b) as a proxy for strain change and compare it with discharge (Fig. 6a). We limit comparison to areas with InSAR coherence exceeding 80%. Least-squares regression



▲ **Figure 6.** Hydrologic response. (a) Map showing percent change in discharge at nine stream gages and well SB01400223BCCD1, Interferometric Synthetic Aperture Radar (InSAR)-derived line of sight displacement and PGA contours. KA, Knik Arm; TA, Turnagain Arm. (b) Discharge before and after the mainshock recorded at U.S. Geological Survey (USGS) well SB01400223BCCD1 (source: see [Data and Resources](#)).

(© Fig. S5b) reveals a weak negative correlation, suggesting that subsidence could have triggered the expulsion of groundwater. However, the correlation is weak and based on a sample size of just six.

Alternatively, strong ground motions may have enhanced streamflow through dynamic mechanisms, including aquifer consolidation, microfracturing, and fracture clearing (e.g., [Manga et al., 2012](#)). We use the PGA (Fig. 2) as a proxy for dynamic strain during the shaking. Least-squares regression shows a positive correlation with PGA at nine gauges (© Fig. S5c). A correlation (negative) also exists with epicentral distance (© Fig. S5d). Both demonstrate that streamflow scales to first order with ground motion, consistent with prior observations (e.g., [Manga and Wang, 2015](#)).

The dataset relating stream discharge to ground motion is stronger than the comparison with subsidence. However, because ground motion and subsidence both decrease as a function of epicentral distance, correlation alone is insufficient to unequivocally separate the influence of the two.

FAILURE OF NATURAL MATERIALS

Two of the authors (R. W. and A. B.) conducted a 225 km overflight the day after the earthquake to assess large ground failures and to help guide subsequent response activities (Fig. 7). This reconnaissance was guided by seismic landslide hazard maps for Anchorage ([Jibson and Michael, 2009](#)) and

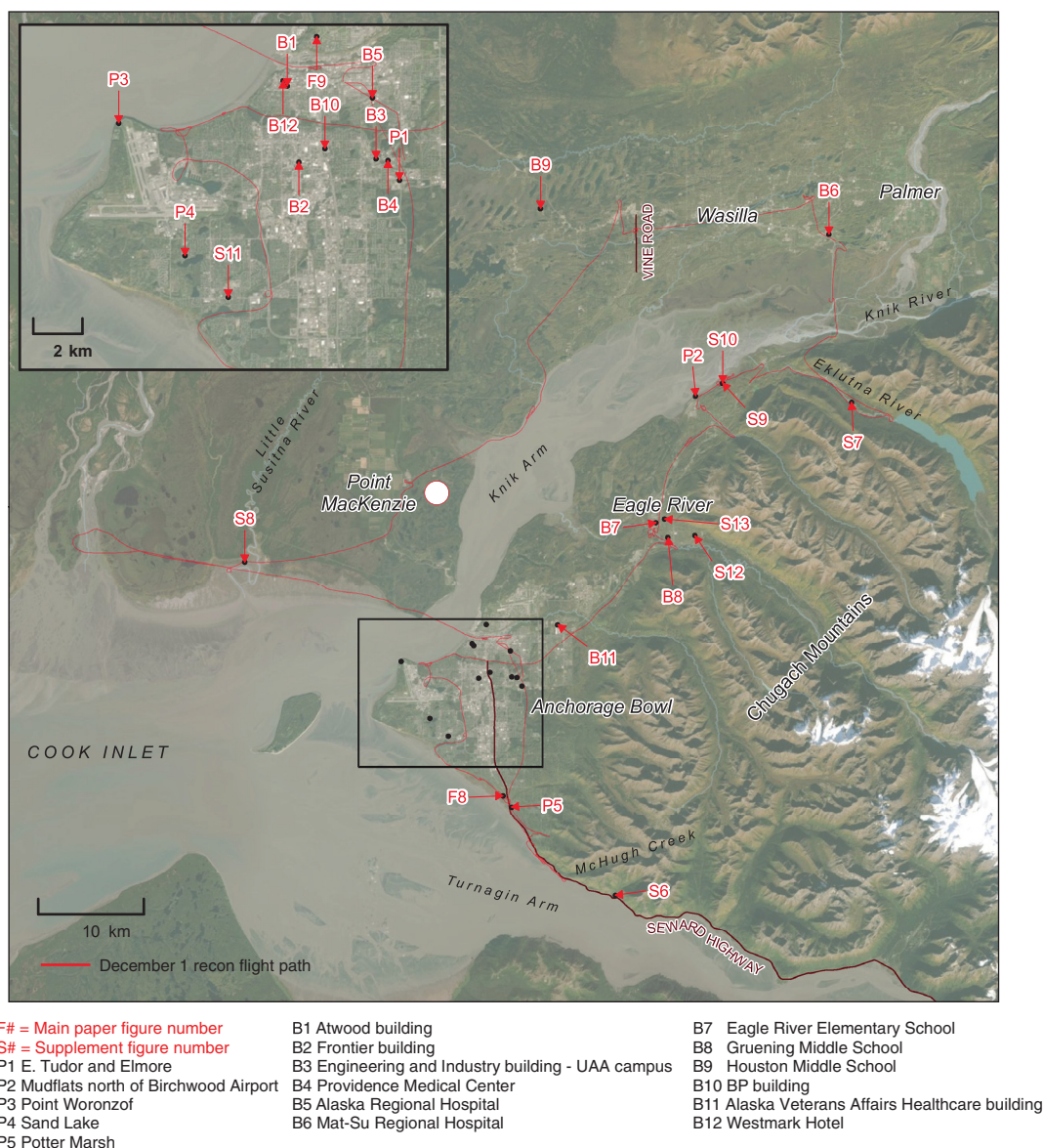
initial estimates of landslide and liquefaction hazard from the USGS ground failure products (see [Data and Resources](#)).

Four categories of ground failures were observed: (1) rockfalls and snow avalanches; (2) slumps, earthflows, and ground cracking in natural materials; (3) debris avalanches on steep walls of river canyons; and (4) liquefaction-related failures. Widespread failures of anthropogenic fill materials were also observed (see the [Failure of Anthropogenic Fill Soils](#) section).

The earthquake shook loose rockfalls and snow avalanches in the Chugach Mountains, which were visible during the initial overflight but obscured by snowfall within a few days. The largest rockfall reported by local eyewitnesses occurred on the southeast face of Rainbow Peak (© Fig. S6). The Chugach National Forest Avalanche Information Center reported earthquake-triggered snow avalanches and rockfalls in alpine terrain surrounding Girdwood (see [Data and Resources](#)). Two large rockfalls also occurred along the Seward Highway between Potter Marsh and McHugh Creek, which resulted in a road closure the day of the earthquake. Although small rockfalls were observed in higher terrain above the Eklutna river and in peaks to the north, no ground failures were observed along the

Chugach mountain range front, where near-real-time ground failure maps had predicted high hazard.

Complex slumping and long-runout earthflows occurred along coastal bluffs in south Anchorage where the ground had failed during prior earthquakes and heavy rainfall. Two- to three-meter-tall headscarps encroached a ~300 m long section of the Alaska Railroad Corporation southern mainline—a single track connecting Anchorage to Seward. This failure destabilized the right of way but caused little damage to the track (Fig. 8). Recurrent landslides, known as the Potter Hill slides, destroyed ~100 m of track and right of way in the same area during the 1964 Great Alaska earthquake ([Hansen, 1965](#)). [Miller and Dobrovolsky \(1959\)](#) reported damage to railroad tracks in the same area after an earthquake in 1954. The first account of landsliding comes from an official of the Alaska railroad, who recalled heavy rains that caused ground failure impacts to hundreds of meters of track in the late 1920s and early 1930s ([Hansen, 1965](#)). D.S. McCulloch and M.G. Bonilla (written comm., 1964, as cited in [Hansen, 1965](#)) describe the composition of the bluffs as till overlying outwash, which in turn overlies blue clay, silt, and fine sand. These layers are similar to the notorious Bootlegger Cove Formation, which was responsible for some of the most extreme soil failures in 1964 ([Miller and Dobrovolsky, 1959](#); [Updike et al., 1988](#)). In 1964, groundwater springs, sourced from permeable beds in the outwash, flowed into ponds that saturate tidal mud flats along the base of the bluff. The 2018 failures appear similar to the slides described in 1964—a series of rotational slump



▲ **Figure 7.** Map of locations referred to throughout the text. P marks places, B marks buildings, F marks figures, and S marks figures in the ⑤ supplemental material. The thin red line marks the route of the 225 km overflight referenced in the [Failure of Natural Materials](#) section.

blocks that disintegrated into earthflows consisting of clay, silt, and sand derived from the lower part of the bluff, the adjacent mudflat, or both. In 1964, McCulloch and Bonilla concluded that bearing strength failure and flowage of materials in the bluff and/or mudflat caused the slides. A similar mechanism probably led to ground failure during this earthquake.

Shallow (<2 m deep) landslides occurred in canyon walls and steep slopes of river valleys where frozen soils shook loose from underlying unconsolidated deposits. Most obvious from the air were debris avalanches on steep slopes underlain by loose Pleistocene sand and gravel at Point Woronzof ([Miller and Dobrovlny, 1959](#); [Schmoll and Dobrovlny, 1972](#)) and Pleistocene glacial gravel, sand, and silt in the Eagle river ([Schmoll et al., 1980](#)) and Eklutna river valleys (⑤ Fig. S7).

The slope failures appeared to be superficial sloughs of frozen, unconsolidated deposits that spread downhill into debris aprons at the base of hillslopes. The slides removed snow on steep slopes and left scars of freshly exposed gravel, sand, and silt, making them easy to distinguish from undisturbed slopes.

Liquefaction-related deformation and venting of saturated sediment occurred beneath tidal flats along Turnagain Arm, Cook Inlet, Knik Arm, and the Little Susitna river delta. The most voluminous liquefaction occurred at the Little Susitna river delta, where sand boils blotted the coastal plain and linear features defined lateral spreading along channel margins (⑤ Fig. S8).

A primary objective of our initial overflight was to assess the potential for reactivation of 1964 ground failures. From the



▲ **Figure 8.** Complex slumping along the Alaska Railroad overlooking the tidal flats of Turnagain Arm, looking northward. Failure of these low bluffs, known as Potter Hill slides (Hansen, 1965), occurred previously during the 1964 Great Alaska earthquake and again during an earthquake in 1954. (61.0874°, -149.84214°). Photo: Adrian Bender.

air, there was no obvious evidence of the movement of large translational slides observed in 1964. We flew over Earthquake Park and along the entire Turnagain Heights landslide that was triggered in 1964 and observed no large displacements at the top of the bluff or bulges along the toe in tidal flats that would have indicated reactivation. Overflights of other areas that moved in 1964 also showed a lack of movement in 2018, including Sunset Park, the former Native Hospital site, and Buttress Park in downtown Anchorage. Because trees obscure the hummocky ground at Earthquake Park, aerial surveys could not rule out the possibility of small (<0.1 m) cracks associated with slide blocks.

To more closely inspect the 1964 landslides, we visited Earthquake Park and Sunset Park on foot four days after the earthquake. These two parks preserve the slide-block landscape that resulted from large translational slides that occurred in 1964, which are comprehensively described by Hansen (1965). At both sites, we observed ~ 0.01 m wide ground cracks along landslide block boundaries and headscarps. One ≤ 0.01 m wide crack at Sunset Park extended ~ 32 m along the headscarp of the translational landslide that destroyed Government Hill Elementary School in 1964 (Fig. 9). Apparently, the duration (20–40 s) and amplitude of strong shaking in the 2018 earthquake stopped short of reactivating large translational landslides that failed previously during much longer (4–5 min) shaking in 1964.

FAILURE OF ANTHROPOGENIC FILL SOILS

One of the main causes of damage to buildings was the permanent movement of soils, sands, and gravels emplaced during

construction projects. We refer to these simply as fill soils. These ground failures can be split into four categories: liquefaction-induced settlement, lateral spreading, settlement not involving liquefaction, and slope displacement.

Liquefaction caused structural damage in several locations in Anchorage. Homeowners with crawl spaces noted piles of fine sand and displaced foundations and utilities. Several residences suffered from settlement of interior concrete floor slabs with fine sand ejecta flowing in through cracks at the edges of the slabs. Sand boils were also noted along sidewalks and roadways in southwestern Anchorage, where groundwater is relatively shallow and subsurface soils consist of sands and gravels (Fig. 10). No direct measurements of liquefaction are available because there are no soil pore water pressure transducer arrays in these areas.

We observed at least one case of lateral spreading near East Tudor Road and Elmore Road in an area where a gravel pit had existed in the 1970s and 1980s and was subsequently backfilled with sand and fine gravel. Surficial cracking and displacements after the earthquake indicated lateral spreading of the shallow slope toward an adjacent artificial pond. We also identified damage to the Alaska Railroad caused by ground failures in artificial materials placed on top of intertidal mudflats northeast of Birchwood Airport. Slumps and saturated earthflows damaged the railroad embankment that abuts and probably overlies natural estuarine silt and sand along the Knik Arm shoreline (© Fig. S9). These ground failures may have initiated in natural materials underlying the railroad embankment. These failures caused the rail line north of Anchorage to close for four days, shutting off rail service to interior Alaska. One of the more famous ground failures of artificial material occurred along Vine Road in Wasilla. Lateral spreading disrupted the road where its artificial embankment crossed a low bog (© Fig. S10). Many failures of engineered materials occurred on or adjacent to saturated lowlands filled with organic sediment, silt, or sand.

Across the region, the majority of the settlement that caused structural damage does not appear to be related to liquefaction, but rather the behavior of uncontrolled fill—defined as fill that may not have been placed and compacted appropriately. © Figure S11 shows an example of this in a neighborhood where fill soils were used to raise homes significantly above street level during construction. Most of the homes in this neighborhood, constructed at the same time, suffered structural damage as a result of settlement near the surface. There were no visible ejecta and groundwater does not approach the surface in this area. These factors suggest that liquefaction did not play a role in the settlement. Instead, these materials may have settled during the earthquake because they were ill-suited for the use or improperly compacted when they were emplaced.

Numerous slope displacements occurred in both urban and rural areas. Notably, very few of these displacements appear to have occurred in natural slopes. Many slopes constructed of fill materials exhibited displacement, with subsequent failures in nearby structures. Observations at several sites indicate that



▲ **Figure 9.** Comparison of ground failure relative to 1964. (a) View to the west showing the Government Hill School collapsed into a graben, or linear trough, formed by the Government Hill landslide in 1964 (Hansen, 1965). (b) Same view in 2013. The graben formed by the landslide is still expressed in the landscape in the lower photo. Photo: Game McGimsey. (c) Crack along headscarp of 1964 slide observed on 4 December 2018. Photo: Rob Witter.

fill soils moved away from structures, causing foundations to settle and crack (© Fig. S12). In areas where structural fill had been placed and properly compacted, little to no displacement was observed. As reconstruction efforts continue, one hypothesis that appears to be true is that the fill slopes that exhibited the largest displacements were constructed with poor-quality fill, were inadequately compacted or poorly designed, or were associated with a combination of factors. A thorough cataloging of observed geotechnical failures can be found in Franke *et al.* (2019).

DAMAGE TO STRUCTURES AND UTILITIES

There is reasonable correlation between the amplitude of shaking and observed damage (Fig. 11, © Fig. S13). In areas such as Sand Lake and downtown Anchorage, there is qualitative agreement between the two. But other areas show less of a relationship. There were few yellow- and red-tagged buildings in

south Anchorage despite having ground motions on par with surrounding areas. This is likely because many buildings in the area are newer one- and two-story wood frame structures.

Although shaking caused some direct structural damage, most damage appears tied to foundation damage resulting from ground failure. Reports of foundation damage in single-family residential buildings are widespread (Fig. 12). A significant percentage of the structural damage occurred in pre-1980 buildings lacking seismic details or in noncode conformant buildings (© Fig. S14). The most common structural damage includes foundation damage, the failure of concrete masonry unit (CMU or cinder blocks) wall-to-floor connections and the buckling of CMU walls (© Fig. S15), deformation and unseating of floor joists, permanent residual drift in one-story residential buildings, diagonal wall cracking in wood and masonry buildings, and walls offset and disconnected from foundations. Less common structural damage included cracks in concrete shear walls and girders, failures in base plates



▲ **Figure 10.** Sand boil, about one foot in length, along a sidewalk in south Anchorage. Photo: Howard Weston.

and foundations for steel braces, cracks in concrete columns, and detachment at the wall corners in residential buildings (Archbold *et al.*, 2018; Hassan *et al.*, 2018). In some instances, the large number of strong aftershocks exacerbated the structural damage. For example, shear cracks in girders at the Westmark Hotel widened from hairline to ~60 mm during aftershocks triggering a seismic retrofit. Some impacts are less easy to inspect and we anticipate hidden structural damage including damage to concrete beam-column connections, cracks punched in concrete flat plates, and yielding in steel columns and older base plates that do not incorporate the design improvements learned from the 1994 Northridge earthquake.

The six buildings in Anchorage that are instrumented with strong-motion seismographs experienced light-to-moderate damage. Most ground-motion spectra recorded at these facilities were below the design earthquake. The 21-story Atwood building, a 1982 building with a steel frame and steel shear walls, was yellow-tagged for considerable flooding and failure of the suspended ceiling grid on three floors. The 14-story Frontier building, a 1981 concrete moment-resisting frame, experienced light nonstructural ceiling and partition wall damage, damage to the elevator counterweight system, and cracks in the concrete cover of exterior and edge columns. The BP building experienced cosmetic nonstructural damage, water flooding, and some structural damage to staircases. The

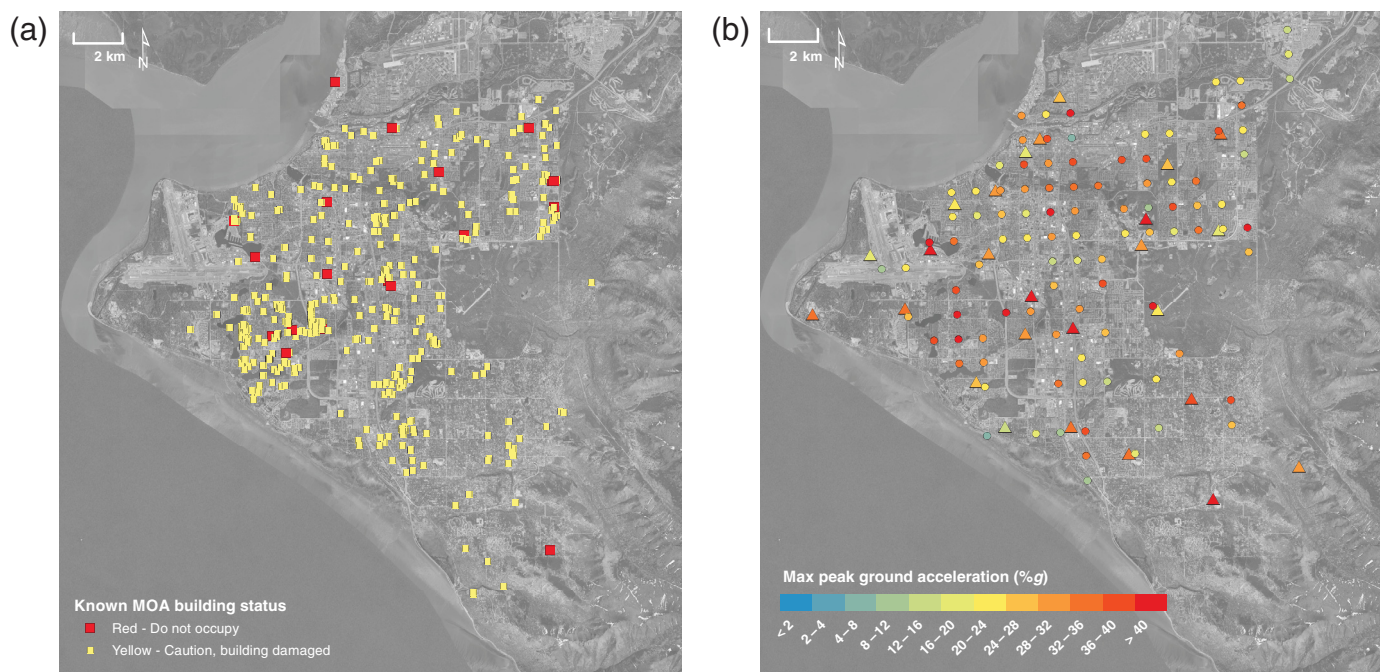
Engineering Building on the University of Alaska Anchorage campus, a 2015 four-story steel moment frame building experienced light cosmetic cracking. The Alaska Veterans Affairs Healthcare building also experienced minor nonstructural damage.

The most common nonstructural damage was the failure of glass facades and windows in low-story retail buildings, tile and grid damage in suspended ceilings, damage to fire-fighting piping and sprinkler systems, and extensive cracking in drywall, partition walls, and masonry veneer. Water boilers proved particularly vulnerable with many instances of pipe failures and subsequent flooding caused by broken restraints and sliding (© Fig. S16).

The three major hospitals in Anchorage experienced light to heavy nonstructural damage, water leaks and flooding, and some equipment damage. The emergency rooms remained open, except for one that was closed briefly to repair water damage. Providence Alaska Hospitals canceled elective surgeries but kept emergency rooms open. Alaska Regional Hospital experienced water flooding because of a failure in the fire-fighting system that forced the shutdown of two outpatient clinic buildings. Two weeks after the earthquake, they were open but still operating at 20%–30% capacity. The Mat-Su Regional Medical Center remained open after the earthquake. One of the hospitals, in a pre-1970 building, experienced shear cracking in the concrete core walls. Another hospital experienced a boiler failure that led to building flooding and an electrical short circuit that activated the fire alarm system. This is an important lesson because the evacuation message conveyed by a fire alarm is directly at odds with the drop, cover, and hold message advocated for earthquake response.

Most schools in the Anchorage and Mat-Su school districts experienced some level of nonstructural damage and closed for one week to allow for inspections, clean up, and repairs (© Fig. S17). Eighty-five of the 97 schools in the Anchorage School District experienced light to heavy nonstructural damage and flooding (see [Data and Resources](#)). Roughly one in five schools in the Anchorage and Mat-Su districts delayed their reopening further to allow time to address minor structural damage. More severe structural damage caused four schools to close for at least a year and potentially permanently. These include two in Eagle River (Eagle River Elementary and Gruening Middle), one school in Anchorage (Alaska Middle College), and one in Mat-Su (Houston Middle). Most of the damage in these schools was to CMU walls and steel beam connections (Archbold *et al.* 2018; Rodgers *et al.* 2019). The geographic distribution of the closed schools is an indication that their damage is attributable to construction and not to a peculiar ground-motion effect in one location.

Damage to the region's inventory of 245 bridges was generally minor, with 20 bridges identified by the Alaska Department of Transportation as having more significant damage (see [Data and Resources](#)). Common bridge damage included shifting girders, damage to shear keys, bent anchor



▲ **Figure 11.** Comparison of building damage and ground motion for the Anchorage Bowl. (a) Original inspection placard value. Source: Municipality of Anchorage Geographic Data and Information Center (last retrieved 26 April 2018). (b) Observed PGA ground motions (triangles) supplemented with PGA values inferred from “Did You Feel It?” (DYFI) reports (circles). See [E](#) Figure S13 for comparable figure for communities to the northeast.

bolts, and damage to the grout pads under bearings ([E](#) Fig. S18). Less common bridge damage included cracks in abutments and settling under approach ramps. The earthquake caused widespread nonstructural damage to highway road paving and substructures. Despite winter conditions pavement damage was generally repaired quickly, though much of this work will be redone at a later date under warmer conditions.

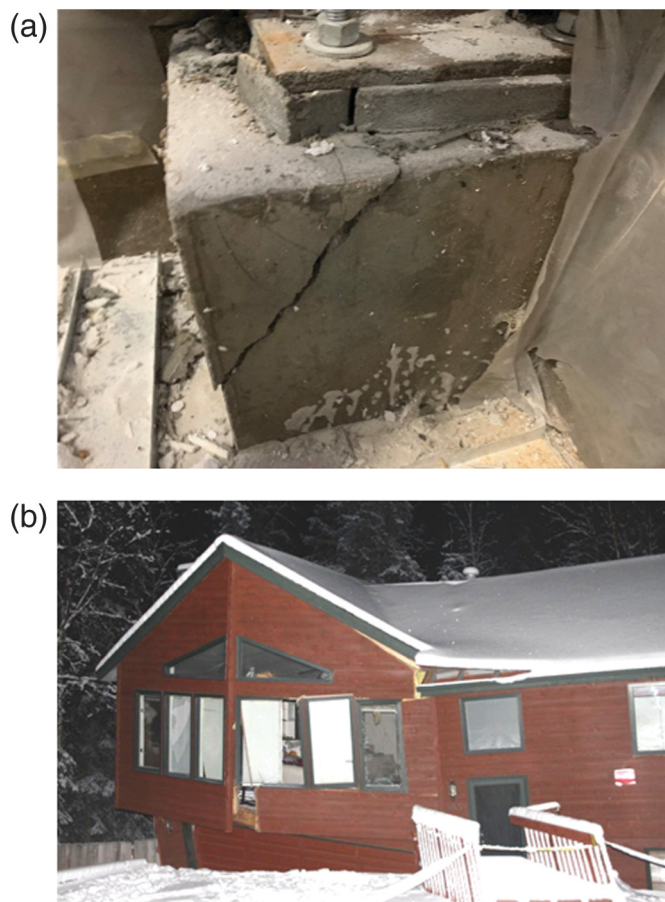
No damage to the trans-Alaska pipeline occurred. At its closest point, the facility is 200 km east of the epicenter. The pipeline was, however, shut down briefly for precautionary inspections. The earthquake caused a wide variety of utility outages, including power and water that impacted thousands of residents. Although the natural gas utility responded to hundreds of reported leaks, there were no significant explosions or fires such as those that occurred after the 2016 *M* 7.1 Iniskin earthquake. During the first couple of hours after the earthquake, many of the major news outlets in the region were offline because of power failures. This slowed the flow of information and complicated initial efforts to assess the impact of the quake. In general, however, most utilities were back online within hours to a few days. Damage in the utility sector was not catastrophic.

DISCUSSION

The 30 November 2018 Anchorage earthquake offers a glimpse into large intraslab earthquakes and our societal response. The earthquake provides a unique set of observations

that can be used to refine ground-motion predictions and hazard models, emergency response procedures, and construction practices. The earthquake also highlights a number of challenges in understanding both the science and the impacts of comparable earthquakes elsewhere.

The Anchorage earthquake occurred within the subducting slab, near the down dip end of a region of flat-slab subduction, and close to the nose of the mantle wedge (Figs. 1, 3). It is unclear whether there is a sliver of mantle above the earthquake source region. If there is, it is still presumably colder and outside of the convective flow of the more substantial parts of the wedge. This is a very different environment than the 2016 *M* 7.1 Iniskin earthquake that occurred 250 km to the southeast at a greater depth of 125 km, adjacent to far hotter mantle and at greater pressures. Earthquakes such as Iniskin are thought to arise, in part, from the volumetric contraction brought on by eclogite phase transitions ([Hacker et al., 2003](#); [Nakajima et al., 2013](#)) beginning around 70 km depth. This metamorphism is thought to compound other plate forces to generate earthquakes at intermediate depths in most of the world's subduction zones ([Astiz et al., 1988](#)). Metamorphic processes are likely responsible for the 100 km depth *M* 7.9 Little Sitkin earthquake in 2014 that occurred farther west in the Rat Islands ([Macpherson and Ruppert, 2015](#)). But the source region of the Anchorage earthquake is too shallow, and potentially too cool, to make a strong argument for metamorphism-driven stresses. The earthquake was located substantially down dip of the 1964 *M* 9.2 rupture zone ([Ichinose et al.,](#)



▲ **Figure 12.** Foundation and structural damage resulting from shifting soils. (a) Cracked concrete footer. Photo: Wael Hassan. (b) House subjected to extreme permanent shear resulting from offsets in the foundation caused by soil failure. Photo: Chris Motter.

2007). Recent slow-slip events have occurred at comparable locations along strike (Fu and Freymueller, 2013). Wech (2016) highlights seismic tremor in this same region. Together these observations indicate that the earthquake was down-dip of the locked zone in a region where slab pull is expected to be a more significant force. The normal-fault mechanism of the mainshock and aftershocks (Fig. 2) aligns strongly with the tensional regime inferred from slab pull. The earthquake also occurred near the depth where the slab transitions from horizontal flat slab motion to more steeply dipping. This bend adds stresses in the slab, although the exact depth of compressional (bottom) versus tensional (top) stresses depends highly on the thickness and rheology of the slab. The fact that the rupture extended toward the top of the slab (Fig. 3) is consistent with the tensional stresses that would be expected in the upper parts of the plate.

The earthquake raised legitimate questions concerning tsunami warnings. The ground displacements for an intraslab earthquake, even a larger one, are too small (Fig. 4) to initiate a tectonic tsunami of consequence. However, strong shaking is capable of initiating subaerial and submarine landslides, which

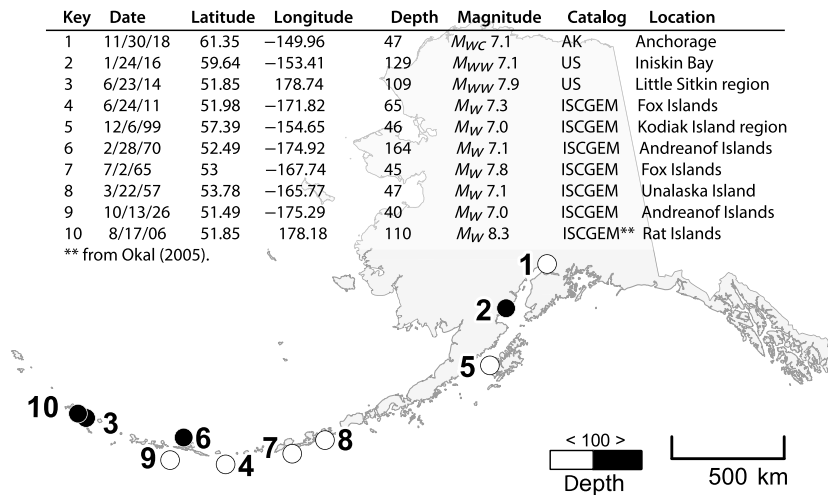
can, in turn, generate tsunamis on a local scale. Landslide-generated tsunamis were a primary contributor to the impacts and casualties of the 1964 earthquake and have been implicated more recently in earthquakes such as the September 2018 M_w 7.5 event in Sulawesi, Indonesia (Sassa and Tomohiro, 2019). Although the steep bluffs and tidal mudflats that are pervasive in the area could have generated subaerial or submarine landslides, these same features offer some protection to coastlines. Residents away from the immediate coastline certainly did not need a tsunami warning, but it is not clear how exactly to treat the coastline itself. Community and agency dialog is needed to better assess how or if tsunami warnings should be issued for highly localized coastal hazards. There is also a clear need for an education campaign to make sure residents are informed of how to respond on their own to strong shaking and where they do and do not need to worry about tsunami inundation. Both of these activities could be facilitated by a comprehensive tsunami hazard evaluation of the area.

Another lesson from this earthquake is the importance of duration and frequency in triggering ground failure. The proximity of Anchorage resulted in strong ground accelerations. However, these motions were dominated by high-frequency energy (Beyzaei *et al.*, 2019) with the strongest shaking lasting just a few tens of seconds. Because of this, the ground velocities and displacements were comparatively smaller than they might have been for a larger more distant earthquake such as the one in 1964. The short duration of strong shaking also meant that soils were not exposed to as many cycles of ground motion as they might have been for other earthquakes with comparable peak accelerations. This fact is not captured by intensity or PGA maps intended to provide a concise regional summary.

After the M 9.2 earthquake and tsunami in 1964, seismic building regulations improved significantly in Alaska. The 1964 earthquake led to seismic policy changes in Alaska and helped pave the way nationwide for better codes and later to the creation of the National Earthquake Hazards Reduction Program in 1977. Alaska has been credited with some of the strictest seismic safety code requirements. These are reflected in local amendments to the International Building Code (IBC), though it should be noted that, for bureaucratic reasons, at the time of the earthquake, the state had adopted only the 2012 IBC and not the more recent 2018 IBC. Even so, the decades of code recognition, combined with building stock in south-central Alaska that is generally less than 30 yr old, created a region with reasonably progressive seismic resilience.

Although strong codes have been in place for decades, the level of enforcement varies widely between the City of Anchorage and many outlying cities and towns, including Eagle River and Girdwood. These communities are part of the Municipality of Anchorage, but code conformance is not mandatory, especially for residential construction.

A few factors are responsible for the overall damage being less than what might have been anticipated. The primary factor is that the depth of the rupture prevented the strongest shaking that would have been expected had the earthquake occurred near the surface. The ground motions did not generally exceed



▲ **Figure 13.** Historical intraslab earthquakes in Alaska, greater or equal to magnitude 7, and 40 km or deeper. The AK, US, and ISCDEM catalogs refer respectively to the catalog of the Alaska Earthquake Center, the USGS Preliminary Determination of Epicenters, and the International Seismological Centre's Global Instrumental Earthquake Catalogue.

that of the design earthquake, although it came close at high frequencies. Damage was also minimized by the relatively short duration of the highest amplitude motions. A third important factor appears to have been the recent history of good construction practices and the relatively young age of the building stock in the region. The fact that no structures collapsed entirely and no one was killed are laudable and is not an accident. We should not overlook, however, the considerable damage and ongoing vulnerabilities caused by nonengineered and pre-1980 construction. The code history described earlier is directly responsible for the relative resilience of the region demonstrated during this earthquake. Even the failures that did occur can generally be associated with ill-fit types of construction or the lack of enforcement (see the [Damage to Structures and Utilities](#) section) and only serve to further validate the building codes where they were followed. The higher rates of building damage outside of the Anchorage Bowl do not appear to correlate with higher ground motions. This argument would be more credible if sufficient instrumental records were available northeast of Anchorage. But the juxtaposition of regions with and without code enforcement provides a rare controlled study. The results of this serendipitous, if unintended, test implies that code enforcement improves earthquake resilience—a conclusion that may not be shocking but is rarely demonstrated so clearly.

Across the Aleutian arc, there have been 10 recorded earthquakes of M 7 or larger below a depth of 40 km since 1906 (see [Data and Resources](#)). These events have been distributed across the 2500 km arc and have occurred, on average, every 11 yr (Figure 13). The largest of these was the M 8.3 event in 1906 (Okal, 2005). Compared with earthquakes on the megathrust, the upper magnitude limits on intraslab earthquakes are smaller. However, intraslab events can occur far

inland from the trench in much closer proximity to population. In this regard, the earthquake is quite similar to the 2017 M 7.1 Puebla-Morelos earthquake near Mexico City (Melgar, Pérez-Campos, *et al.*, 2018; Sahakian *et al.*, 2018).

Of the three primary contributors to seismic hazard in southern Alaska—the intraslab region, the subduction megathrust, and the continental crust—intraslab earthquakes are the most difficult to quantify in probabilistic terms. Unlike faults that rupture the surface, geologic features cannot be used to estimate fault length or slip rate. Because the slab is decoupled from the overriding continental plate, geodetic motions on the surface similarly have little relation to deformation within the slab. Lake paleoseismology is one potential approach for evaluating the frequency of intraslab earthquakes. Turbidites and sublacustrine landslides in lake sediments can be an indicator of strong shaking. If the crust and megathrust

earthquake record is sufficiently understood, it could be possible to attribute the remaining sediment features to earthquakes occurring in the slab (Praet *et al.*, 2017; Boes *et al.*, 2018; Fortin *et al.*, 2019).

Even historical seismicity is a marginal indicator of the hazard. The brief historical record in the Anchorage region is insufficient to constrain probabilities. For much of the earthquake record prior to the mid-twentieth century, questionable location and source mechanism information make it difficult to distinguish between neighboring, but very different, source regions. Silwal *et al.* (2018) propose an intraslab source for the 1954 M_w 6.4 earthquake that occurred 75 km southwest of Anchorage. However, the authors state that the data cannot entirely rule out a source on the subduction interface. The earthquakes in Figure 13 support only rudimentary statistical consideration assuming large intermediate depth earthquakes are distributed evenly across the arc. A systematic comparison of slab properties and focal mechanisms might shed insight on where such events are unlikely. However, focal mechanisms (and reliable depths) are only available for the most recent of these earthquakes. A more fruitful approach may be to use this small sample of events to calibrate against global observations of comparable earthquakes. But this brings challenges in reconciling the properties of different subduction zones. Barring explicit knowledge of the cause of the different earthquakes in Figure 13, there is no evidence to rule out an event such as the 1906 M 8.3 earthquake occurring under southcentral Alaska.

The Anchorage earthquake is unlikely to cause a significant reevaluation of the fundamental processes occurring within subducting plates. It should, however, serve as a stern reminder of the importance of accounting for intraslab earthquakes, despite their challenges, in seismic hazard analyses. And for an area that has not experienced comparable shaking in half a century, it serves as a reminder of why seismically informed

construction matters, what we have done well over the past few decades, and where we still need work.

DATA AND RESOURCES

All seismic waveform data are available through the Incorporated Research Institutions for Seismology (IRIS) Data Management Center (<https://ds.iris.edu/ds/nodes/dmc>). Strong-motion seismic records are available from the Center for Strong Motion Engineering Data (<https://strongmotioncenter.org>). The catalog of Alaska earthquakes is distributed through the Advanced National Seismic System (ANSS) Composite Catalog (<https://earthquake.usgs.gov/data/comcat>). Interferometric Synthetic Aperture Radar (InSAR) data available through the SARVIEWS project (sarviews-hazards.alaska.edu). Hydrology distributed at <https://waterdata.usgs.gov>. Photographs of damage and soil failures, as well as accompanying descriptions, are courtesy of the photographer, as noted. The building damage database is available from the Municipality of Anchorage. Full data and parameters used to derive the ground acceleration contours in Figure 2 are available at <http://earthquake.alaska.edu/event/20419010/shakemap>. Tsunami warning for the coastlines of Cook Inlet and the southern Kenai Peninsula is available at <https://tsunami.gov/events/PAAQ/2018/11/30/pj004/1/WEAK51/WEAK51.txt>. Advanced National Seismic System (ANSS) ComCat portal information is available at <https://earthquake.usgs.gov/earthquakes/eventpage/ak20419010/shakemap>. U.S. Geological Survey (USGS) ground failure products are available at <https://earthquake.usgs.gov/earthquakes/eventpage/ak20419010/ground-failure>. The Chugach National Forest Avalanche Information Center is available at <http://www.cnfaic.org/site/observations/rainbow-peak>. Anchorage School District earthquake reporting is available at <https://www.asdk12.org/2018earthquake>. Alaska earthquake damage assessment updates are available at <http://dot.alaska.gov/earthquake2018>. USGS current water data for Alaska are available at waterdata.usgs.gov/ak/nwis/rt. The © supplemental material for this article includes methodological descriptions, tables with supporting details, figures that illustrate various discussion points, and photographs that provide examples for some of the observations presented in the article. All websites were last accessed September 2019. ☒

ACKNOWLEDGMENTS

This article builds on the observations and efforts of a wide range of individuals and funding sources. This article benefited from careful reviews by Honn Kao, Brian Sherrod, and three anonymous reviewers. The authors thank the Earthquake Engineering Research Institute for coordinating routine conference calls in the days after the earthquake. These calls improved the quality and depth of observations, especially in the short window of time before winter weather obscured ground observations. Janise Rodgers and Chris Motter were instrumental in gathering information on Matanuska–Susitna (Mat-Su) schools. This research was supported in part by the Office of Alaska State Seismologist (L. G., M. G., N. R., and

M. W.) and the National Science Foundation Award Number EAR 1251971 (C. R. and C. T.). Any use of trade, firm, or product names is for descriptive purposes only and does not imply endorsement by the U.S. Government.

REFERENCES

- Abers, G. A. (2008). Orogenesis from subducting thick crust and evidence from Alaska, in *Active Tectonics and Seismic Potential in Alaska*, J. T. Freymueller, P. J. Haeussler, R. Wesson, and G. Ekström (Editors), Geophysical Monograph Series, Vol. 179, American Geophysical Union, Washington, D.C., 337–349.
- Ajadi, O., F. J. Meyer, and P. W. Webley (2016). Change detection in synthetic aperture radar images using a multiscale-driven approach, *Remote Sens.* **8**, no. 6, 482, doi: [10.3390/rs8060482](https://doi.org/10.3390/rs8060482).
- Archbold, J., W. M. Hassan, T. Kijewski-Correa, J. Marshall, G. P. Mavroedidis, K. M. Mosalam, S. Muin, H. Mulchandani, H. Peng, and R. Pretell (2018). *StEER & EERI Alaska Earthquake Preliminary Virtual Assessment Team (P-VAT) Joint Report*, D. Prevatt, D. Roueche, and I. Robertson (Editors), Earthquake Engineering Research Institute (EERI), Oakland, California, available at http://www.learningfromearthquakes.org/2018-11-30-anchorage-alaska/images/2018_11_30_Anchorage_Alaska/pdf/StEER_Alaska_Earthquake_-_P-VAT_Report.pdf (last accessed September 2019).
- Astiz, L., T. Lay, and H. Kanamori (1988). Large intermediate-depth earthquakes and the subduction process, *Phys. Earth Planet. In.* **53**, nos. 1/2, 80–166, doi: [10.1016/0031-9201\(88\)90138-0](https://doi.org/10.1016/0031-9201(88)90138-0).
- Beyzaei, C. Z., A. Cabas, S. Dow, K. Franke, M. Freeman, R. Koehler, K. Lee, G. Pierce, I. Pierce, A. Stuedlein, and Z. Yang (2019). Geotechnical Engineering Reconnaissance of the 30 November 2018 Mw 7.0 Anchorage, *Alaska Earthquake Version 1.0*, Geotechnical Extreme Events Reconnaissance Association (GEER), 50 pp., doi: [10.18118/G6P07F](https://doi.org/10.18118/G6P07F).
- Boes, E., M. Van Daele, J. Moernaut, S. Schmidt, B. J. Jensen, N. Praet, D. Kaufman, P. Haeussler, M. G. Loso, and M. De Batist (2018). Varve formation during the past three centuries in three large proglacial lakes in south-central Alaska, *Geol. Soc. Am. Bull.* **130**, nos. 5/6, 757–774.
- Boore, D. M., J. P. Stewart, E. Seyhan, and G. M. Atkinson (2014). NGA-West2 equations for predicting PGA, PGV, and 5% damped PSA for shallow crustal earthquakes, *Earthq. Spectra* **30**, no. 3, 1057–1085, doi: [10.1193/070113EQS184M](https://doi.org/10.1193/070113EQS184M).
- Burdick, S., F. L. Vernon, V. Martynov, J. Eakins, T. Cox, J. Tytell, T. Mulder, M. C. White, L. Astiz, G. L. Pavlis, and R. D. van der Hilst (2017). Model update May 2016: Upper-mantle heterogeneity beneath North America from travel-time tomography with global and USArray data, *Seismol. Res. Lett.* **88**, no. 2A, 319–325.
- Caprio, M., B. Tarigan, C. B. Worden, S. Wiemer, and D. J. Wald (2015). Ground motion to intensity conversion equations (GMICEs): A global relationship and evaluation of regional dependency, *Bull. Seismol. Soc. Am.* **105**, no. 3, 1476–1490, doi: [10.1785/0120140286](https://doi.org/10.1785/0120140286).
- Christeson, G. L., S. P. S. Gulick, H. J. A. van Avendonk, L. L. Worthington, R. S. Reece, and T. L. Pavlis (2010). The Yakutat terrane: Dramatic change in crustal thickness across the transition fault, Alaska, *Geology* **38**, 895–898.
- Department of Commerce, National Oceanic & Atmospheric Administration, National Weather Service (2009). *National Weather Service Instruction 10-701*, Tsunami Warning Center Services, NWSPD 10–7, available at <https://www.nws.noaa.gov/directives/010/archive/pd01007001c.pdf> (last accessed September 2019).
- Dutta, U., M. K. Sen, N. Biswas, and Z. Yang (2009). Investigation of shallow sedimentary structure of the Anchorage basin, Alaska, using

- simulated annealing inversion of site response, *Bull. Seismol. Soc. Am.* **99**, no. 1, 326–339, doi: [10.1785/0120070250](https://doi.org/10.1785/0120070250).
- Eberhart-Phillips, D., D. H. Christensen, T. M. Brocher, R. Hansen, N. A. Ruppert, P. J. Haeussler, and G. A. Abers (2006). Imaging the transition from Aleutian subduction to Yakutat collision in central Alaska, with local earthquakes and active source data, *J. Geophys. Res.* **111**, no. B11, doi: [10.1029/2005JB004240](https://doi.org/10.1029/2005JB004240).
- Eberhart-Phillips, D., P. J. Haeussler, J. T. Freymueller, A. D. Frankel, C. M. Rubin, P. Craw, N. A. Ratchkovski, G. Anderson, G. A. Carver, A. J. Crone, *et al.* (2003). The 2002 Denali fault earthquake, Alaska: A large magnitude, slip-partitioned event, *Science* **300**, no. 5622, 1113–1118, doi: [10.1126/science.1082703](https://doi.org/10.1126/science.1082703).
- Eberhart-Phillips, D., A. Nayak, N. Ruppert, and C. Thurber (2019). Alaska 2018 update for USGS G18AP00017: Initial Development of Alaska Community Seismic Velocity Models, *Zenodo*, doi: [10.5281/ZENODO.2544925](https://doi.org/10.5281/ZENODO.2544925).
- Ferris, A., G. A. Abers, D. H. Christensen, and E. Veenstra (2003). High resolution image of the subducted Pacific (?) plate beneath central Alaska, 50–150 km depth, *Earth Planet. Sci. Lett.* **214**, nos. 3/4, 575–588, doi: [10.1016/S0012-821X\(03\)00403-5](https://doi.org/10.1016/S0012-821X(03)00403-5).
- Fortin, D., N. Praet, N. P. McKay, D. S. Kaufman, B. J. Jensen, P. J. Haeussler, C. Buchanan, and M. De Batist (2019). New approach to assessing age uncertainties—The 2300-year varve chronology from Eklutna Lake, Alaska (USA), *Quaternary Sci. Rev.* **203**, 90–101.
- Franke, K. W., R. D. Koehler, C. Z. Beyzaei, A. Cabas, I. Pierce, A. Stuedlein, and Z. Yang (2019). Geotechnical engineering reconnaissance of the 30 November 2018 Mw 7.0 Anchorage, Alaska Earthquake, *GEER Rept. GEER-059*, Geotechnical Extreme Events Association, 1 pp., doi: [10.18118/G6P07F](https://doi.org/10.18118/G6P07F).
- Fu, Y., and J. T. Freymueller (2013). Repeated large slow slip events at the southcentral Alaska subduction zone, *Earth Planet. Sci. Lett.* **375**, 303–311, doi: [10.1016/j.epsl.2013.05.049](https://doi.org/10.1016/j.epsl.2013.05.049).
- González, F. I., B. L. Sherrod, B. F. Atwater, A. P. Frankel, S. P. Palmer, M. L. Holmes, R. E. Karlin, B. E. Jaffe, V. V. Titov, H. O. Mofjeld, and A. J. Venturato (2003). *Puget Sound Tsunami Sources—2002 Workshop Report*, NOAA/Pacific Marine Environmental Laboratory Contribution No. 2526, 36 pp.
- Grapenthin, R., M. West, C. Tape, M. Gardine, and J. T. Freymueller (2018). Single-frequency instantaneous GNSS velocities resolve dynamic ground motion of the 2016 Mw 7.1 Iniskin, Alaska, earthquake, *Seismol. Res. Lett.* **89**, no. 3, 1040–1048, doi: [10.1785/0220170235](https://doi.org/10.1785/0220170235).
- Hacker, B. R., S. M. Peacock, G. A. Abers, and S. D. Holloway (2003). Subduction factory 2. Are intermediate-depth earthquakes in subducting slabs linked to metamorphic dehydration reactions?, *J. Geophys. Res.* **108**, no. B1, doi: [10.1029/2001jb001129](https://doi.org/10.1029/2001jb001129).
- Haeussler, P. J. (2008). An overview of the neotectonics of interior Alaska: Far-field deformation from the Yakutat microplate collision, in *Active Tectonics and Seismic Potential in Alaska*, J. T. Freymueller, P. J. Haeussler, R. Wesson, and G. Ekström (Editors), Geophys. Monogr. Ser., Vol. 179, American Geophysical Union, Washington, D.C., 83–108, doi: [10.1029/179GM05](https://doi.org/10.1029/179GM05).
- Hansen, W. R. (1965). Effects of the earthquake of March 27, 1964, at Anchorage, Alaska, *U.S. Geol. Surv. Profess. Pap.* (542-A), 68 pp.
- Hassan, W., E. Fischer, M. Hakhmaneshi, J. Gaitan, R. Pretell, B. Ong, L. Laughery, N. Paul, D. Yoo, Y. Alberto, *et al.* (2018). Phase I response to M7.0 Anchorage, Alaska earthquake, Nov 30, 2018, in *VERT: Virtual Earthquake Reconnaissance Report*, Earthquake Engineering Research Institute (EERI), Oakland, California, available at http://www.learningfromearthquakes.org/2018-11-30-anchorage-alaska/images/2018_11_30_Anchorage_Alaska/pdf/181203-VERT-Phase-1-Alaska-M7.0-EQ.pdf (last accessed September 2019).
- Hayes, G. P., G. L. Moore, D. E. Portner, M. Hearne, H. Flamme, M. Furtney, and G. M. Smoczyk (2018). Slab2, a comprehensive subduction zone geometry model, *Science* **362**, no. 6410, 58–61, doi: [10.1126/science.aat4723](https://doi.org/10.1126/science.aat4723).
- Huang, P. Y., P. Whitmore, D. Nyland, and A. Medbery (2007). West Coast and Alaska tsunami warning center global earthquake detection system, presented at *2007 AGU Fall Meeting*, San Francisco, California, 10–14 December, abstract S53A-1025.
- Ichinose, G., P. Somerville, H. K. Thio, R. Graves, and D. O'Connell (2007). Rupture process of the 1964 Prince William Sound, Alaska, earthquake from the combined inversion of seismic, tsunami, and geodetic data, *J. Geophys. Res.* **112**, no. 7, 1–21, doi: [10.1029/2006JB004728](https://doi.org/10.1029/2006JB004728).
- Jiang, C., B. Schmandt, K. M. Ward, F. C. Lin, and L. L. Worthington (2018). Upper mantle seismic structure of Alaska from Rayleigh and S-wave tomography, *Geophys. Res. Lett.* **45**, no. 19, 10,350–10,359, doi: [10.1029/2018GL079406](https://doi.org/10.1029/2018GL079406).
- Jibson, R. W., and J. A. Michael (2009). Maps showing seismic landslide hazards in Anchorage, Alaska, *U.S. Geol. Surv. Sci. Invest. Map* 3077, scale 1:25, 000, 11 pp. pamphlet, available at <http://pubs.usgs.gov/sim/3077> (last accessed September 2019).
- Kim, Y., G. A. Abers, J. Li, D. Christensen, J. Calkins, and S. Rondenay (2014). Alaska megathrust 2: Imaging the megathrust zone and Yakutat/Pacific plate interface in the Alaska subduction zone, *J. Geophys. Res.* **119**, no. 3, 1924–1941.
- Lander, J. F. (1996). Tsunamis affecting Alaska, 1737–1996, *National Geophysical Data Center (NGDC) Key to Geophysical Research Documentation*, National Oceanic and Atmospheric Administration, Boulder, Colorado, 31 pp., available at <ftp://ftp.ngdc.noaa.gov/hazards/publications/Kgrd-31.pdf> (last accessed September 2019).
- Liu, C., T. Lay, Z. Xie, and X. Xiong (2019). Intralab deformation in the 30 November 2018 Anchorage, Alaska, MW 7.1 earthquake, *Geophys. Res. Lett.* **46**, no. 5, 2449–2457, doi: [10.1029/2019GL082041](https://doi.org/10.1029/2019GL082041).
- Lu, Z., T. Wright, and C. Wicks (2003). Deformation of the 2002 Denali Fault Earthquakes, mapped by Radarsat-1 interferometry, *Eos Trans. AGU* **84**, no. 41, 425, doi: [10.1029/2003EO410002](https://doi.org/10.1029/2003EO410002).
- Macpherson, K. A., and N. A. Ruppert (2015). Evidence of Wadati–Benioff zone triggering following the Mw 7.9 Little Sitkin, Alaska intermediate depth earthquake of 23 June 2014, *Geophys. Res. Lett.* **42**, no. 15, 6269–6277, doi: [10.1002/2015GL065023](https://doi.org/10.1002/2015GL065023).
- Manga, M. (2001). Origin of postseismic streamflow changes inferred from baseflow recession and magnitude-distance relations, *Geophys. Res. Lett.* **28**, 2133–2136, doi: [10.1029/2000GL012481](https://doi.org/10.1029/2000GL012481).
- Manga, M., and C. Y. Wang (2015). Earthquake hydrology, in *Treatise on Geophysics*, G. Schubert (Editor), Vol. 4, no. 2, Elsevier, Amsterdam, The Netherlands, 305–328, doi: [10.1016/B978-0-444-53802-4.00082-8](https://doi.org/10.1016/B978-0-444-53802-4.00082-8).
- Manga, M., I. Beresnev, E. E. Brodsky, J. Elkhoury, D. Elsworth, S. E. Ingebritsen, D. Mays, and C. Y. Wang (2012). Changes in permeability by transient stresses: Field observations, experiments and mechanisms, *Rev. Geophys.* **50**, no. 2, doi: [10.1029/2011RG000382](https://doi.org/10.1029/2011RG000382).
- Martin-Short, R., R. Allen, I. D. Bastow, R. W. Porritt, and M. S. Miller (2018). Seismic imaging of the Alaska subduction zone: Implications for slab geometry and volcanism, *Geochim. Geophys. Res.* **19**, no. 11, 4541–4560, doi: [10.1029/2018GC007962](https://doi.org/10.1029/2018GC007962).
- Martirosyan, A., U. Dutta, N. Biswas, A. Papageorgiou, and R. Combellick (2002). Determination of site response in Anchorage, Alaska, on the basis of spectral ratio methods, *Earthq. Spectra* **18**, no. 1, 85–104, doi: [10.1193/1.1464535](https://doi.org/10.1193/1.1464535).
- Melgar, D., X. Pérez-Campos, L. Ramirez-Guzmán, Z. Spica, V. H. Espíndola, W. C. Hammond, and E. Cabral-Cano (2018). Bend faulting at the edge of a flat slab: The 2017 Mw 7.1 Puebla-Morelos, Mexico earthquake, *Geophys. Res. Lett.* **45**, no. 6, 2633–2641, doi: [10.1002/2017GL076895](https://doi.org/10.1002/2017GL076895).
- Melgar, D., A. Ruiz-Angulo, E. S. García, M. Manea, V. C. Manea, X. Xu, M. T. Ramirez-Herrera, J. Zavala-Hidalgo, J. Geng, N. Corona, *et al.* (2018). Deep embrittlement and complete rupture of the lithosphere during the Mw 8.2 Tehuantepec earthquake, *Nature Geosci.* **11**, no. 12, 955–960, doi: [10.1038/s41561-018-0229-y](https://doi.org/10.1038/s41561-018-0229-y).

- Meyer, F. J., D. B. McAlpin, W. Gong, O. Ajadi, S. Arko, P. W. Webley, and J. Dehn (2015). Integrating SAR and derived products into operational volcano monitoring and decision support systems, *ISPRS J. Photogram. Remote Sens.* **100**, 106–117, doi: [10.1016/j.isprsjprs.2014.05.009](https://doi.org/10.1016/j.isprsjprs.2014.05.009).
- Miller, M. S., L. J. O'Driscoll, R. W. Porritt, and S. M. Roeske (2018). Multiscale crustal architecture of Alaska inferred from P receiver functions, *Lithosphere* **10**, no. 2, 267–278, doi: [10.1130/L701.1](https://doi.org/10.1130/L701.1).
- Miller, R. D., and E. Dobrovolsky (1959). Surficial geology of Anchorage and vicinity, Alaska, *U.S. Geol. Surv. Bull.* 1093, 128 pp., 1 pl., scale 1:63,360.
- Montgomery, D. R., and M. Manga (2003). Streamflow and water well responses to earthquakes, *Science* **300**, 2047–2049, doi: [10.1126/science.1082980](https://doi.org/10.1126/science.1082980).
- Nakajima, J., N. Uchida, T. Shiina, A. Hasegawa, B. R. Hacker, and S.H. Kirby (2013). Intermediate-depth earthquakes facilitated by eclogitization-related stresses, *Geology* **41**, no. 6, 659–662, doi: [10.1130/g33796.1](https://doi.org/10.1130/g33796.1).
- Okal, E. A. (2005). A re-evaluation of the great Aleutian and Chilean earthquakes of 1906 August 17, *Geophys. J. Int.* **161**, no. 2, 268–282, doi: [10.1111/j.1365-246X.2005.02582.x](https://doi.org/10.1111/j.1365-246X.2005.02582.x).
- Okal, E. A., and B. A. Romanowicz (1994). On the variation of *b*-values with earthquake size, *Phys. Earth Planet. In.* **87**, nos. 1/2, 55–76, doi: [10.1016/0031-9201\(94\)90021-3](https://doi.org/10.1016/0031-9201(94)90021-3).
- Potin, P., B. Rosich, J. Roeder, and P. Bargellini (2014). Sentinel-1 mission operations concept, *IEEE Geoscience and Remote Sensing Symposium*, IEEE, 1465–1468, doi: [10.1109/IGARSS.2014.6946713](https://doi.org/10.1109/IGARSS.2014.6946713).
- Praet, N., J. Moernaut, M. Van Daele, E. Boes, P. J. Haeussler, M. Strupler, S. Schmidt, M. G. Loso, and M. De Batist (2017). Paleoseismic potential of sublacustrine landslide records in a high-seismicity setting (south-central Alaska), *Mar. Geol.* **384**, 103–119.
- Rodgers, J., W. Hassan, C. Motter, and J. Thornley (2019). Impacts on school resilience caused by the M7.1 November 30, 2018 Anchorage earthquake, *Seismological Society of America Annual Meeting*, Seattle, Washington, 23–26 April.
- Ruppert, N. A. (2008). Stress map for Alaska from earthquake focal mechanisms, in *Active Tectonics and Seismic Potential in Alaska*, J. T. Freymueller, P. J. Haeussler, R. Wesson, and G. Ekström (Editors), Geophysics Monograph Series, Vol. 179, American Geophysical Union, Washington, D.C., 351–367, doi: [10.1029/179GM20](https://doi.org/10.1029/179GM20).
- Ruppert, N. A., C. Rollins, A. Zhang, L. Meng, S. G. Holtkamp, M. E. West, and J. T. Freymueller (2018). Complex faulting and triggered rupture during the 2018 MW 7.9 Offshore Kodiak, Alaska, earthquake, *Geophys. Res. Lett.* **45**, no. 15, 7533–7541, doi: [10.1029/2018GL078931](https://doi.org/10.1029/2018GL078931).
- Sahakian, V. J., D. Melgar, L. Quintanar, L. Ramírez-Guzmán, X. Pérez-Campos, and A. Baltay (2018). Ground motions from the 7 and 19 September 2017 Tehuantepec and Puebla-Morelos, Mexico, earthquakes, *Bull. Seismol. Soc. Am.* **108**, no. 6, 3300–3312, doi: [10.1785/0120180108](https://doi.org/10.1785/0120180108).
- Sassa, S., and T. Tomohiro (2019). Liquefied gravity flow-induced tsunami: First evidence and comparison from the 2018 Indonesia Sulawesi earthquake and tsunami disasters, *Landslides* **16**, no. 1, 195–200, doi: [10.1007/s10346-018-1114-x](https://doi.org/10.1007/s10346-018-1114-x).
- Schmoll, H. R., and E. Dobrovolsky (1972). Generalized geologic map of Anchorage and vicinity, Alaska, *U.S. Geol. Surv. Misc. Geol. Invest. Map I-787-A*, 1 sheet, scale 1:24,000.
- Schmoll, H. R., E. Dobrovolsky, and C. A. Gardener (1980). Preliminary geologic map of the Middle Part of the Eagle River Valley, Municipality of Anchorage, Alaska, *U.S. Geol. Surv. Open-File Rept.* 80-890, 11 pp., 1 pl., scale 1:25,000.
- Silwal, V., and C. Tape (2016). Seismic moment tensors and estimated uncertainties in southern Alaska, *J. Geophys. Res.* **121**, 2772–2797, doi: [10.1002/2015JB012588](https://doi.org/10.1002/2015JB012588).
- Silwal, V., C. Tape, and A. Lomax (2018). Crustal earthquakes in the Cook Inlet and Susitna region of southern Alaska, *Tectonophysics* **745**, 243–263, doi: [10.1016/j.tecto.2018.08.013](https://doi.org/10.1016/j.tecto.2018.08.013).
- Udipke, R. G., J. A. Egan, Y. Moriawaki, I. M. Idriss, and T. L. Moses (1988). A model for earthquake-induced translatory landslides in Quaternary sediments, *Geol. Soc. Am. Bull.* **100**, no. 5, 783–792, doi: [10.1130/0016-7606\(1988\)100<0783:AMFEIT>2.3.CO;2](https://doi.org/10.1130/0016-7606(1988)100<0783:AMFEIT>2.3.CO;2).
- Wald, D. J., and T. I. Allen (2007). Topographic slope as a proxy for seismic site conditions and amplification, *Bull. Seismol. Soc. Am.* **97**, no. 5, 1379–1395.
- Waldhauser, F., and W. L. Ellsworth (2000). A double-difference location algorithm: Method and application to the northern Hayward fault, California, *Bull. Seismol. Soc. Am.* **90**, 1353–1368.
- Wang, D., N. C. Becker, S. Weinstein, Z. Duputel, L. A. Rivera, G. P. Hayes, B. F. Hirshorn, R. H. Bouchard, and G. Mungov (2017). Evaluation of W phase CMT based PTWC real-time tsunami forecast model using DART observations: Events of the last decade, presented at *2017 AGU Fall Meeting*, New Orleans, Louisiana, 11–15 December.
- Wech, A. G. (2016). Extending Alaska's plate boundary: Tectonic tremor generated by Yakutat subduction, *Geology* **44**, no. 7, 587–590, doi: [10.1130/G37817.1](https://doi.org/10.1130/G37817.1).
- Whitmore, P., H. Benz, M. Bolton, G. Crawford, L. Dengler, G. Fryer, J. Goltz, R. Hansen, K. Kryzanowski, S. Malone, et al. (2008). NOAA/West Coast and Alaska tsunami warning center Pacific Ocean response criteria, *Sci. Tsunami Haz.* **27**, no. 2, 1–19.
- Worden, C. B., M. C. Gerstenberger, D. A. Rhoades, and D. J. Wald (2012). Probabilistic relationships between ground-motion parameters and modified Mercalli intensity in California, *Bull. Seismol. Soc. Am.* **102**, no. 1, 204–221, doi: [10.1785/0120110156](https://doi.org/10.1785/0120110156).
- Wright, T. J., Z. Lu, and C. Wicks (2003). Source model for the Mw 6.7, 23 October 2002, Nenana Mountain Earthquake (Alaska) from InSAR, *Geophys. Res. Lett.* **30**, no. 18, doi: [10.1029/2003GL018014](https://doi.org/10.1029/2003GL018014).
- Yue, H., T. Lay, J. T. Freymueller, K. Ding, L. Rivera, N. A. Ruppert, and K. D. Koper (2013). Supershear rupture of the 5 January 2013 Craig, Alaska (Mw 7.5) earthquake, *J. Geophys. Res.* **118**, no. 11, 5903–5919, doi: [10.1002/2013JB010594](https://doi.org/10.1002/2013JB010594).
- Zhao, J. X., J. Zhang, A. Asano, Y. Ohno, T. Oouchi, T. Takahashi, H. Ogawa, K. Irikura, H. K. Thio, P. G. Somerville, et al. (2006). Attenuation relations of strong ground motion in Japan using site classification based on predominant period, *Bull. Seismol. Soc. Am.* **96**, no. 3, 898–913, doi: [10.1785/0120050122](https://doi.org/10.1785/0120050122).
- Zhu, L., and D. Helmberger (1996). Advancement in source estimation techniques using broad-band regional seismograms, *Bull. Seismol. Soc. Am.* **86**, no. 5, 1634–1641.

Michael E. West

Matthew Gardine

Lea Gardine

Franz Meyer

Natalia Ruppert

Carl Tape¹

Geophysical Institute

University of Alaska Fairbanks

2156 Koyukuk Drive

Fairbanks, Alaska 99775 U.S.A.

mewest@alaska.edu

mgardin2@alaska.edu

lagardine@alaska.edu

fjmeyer@alaska.edu

naruppert@alaska.edu

ctape@alaska.edu

*Adrian Bender
Peter Haeussler
Rob Witter
Alaska Science Center
U.S. Geological Survey
4210 University Drive
Anchorage, Alaska 99508 U.S.A.
abender@usgs.gov
pheuslr@usgs.gov
rwitter@usgs.gov*

*Kara Gately
National Tsunami Warning Center
910 S Felton Street
Palmer, Alaska 99645 U.S.A.
Kara.Gately@noaa.gov*

*Wael Hassan
Civil Engineering Department
University of Alaska Anchorage
3211 Providence Drive
Anchorage, Alaska 99508 U.S.A.
wmhassan@alaska.edu*

*Cole Richards
Department of Geosciences
University of Alaska Fairbanks
900 Yukon Drive
Fairbanks, Alaska 99775 U.S.A.
csrichards2@alaska.edu*

*John Thornley
Golder Associates Inc.
2121 Abbott Road
Anchorage, Alaska 99507 U.S.A.
john_thornley@golder.com*

Published Online 16 October 2019

¹ Also at Department of Geosciences, University of Alaska Fairbanks, 900 Yukon Drive, Fairbanks, Alaska 99775 U.S.A.

Supplemental Content to

The 30 November 2018 $M_w7.1$ Anchorage Earthquake

By Michael E. West, Adrian Bender, Matthew Gardine, Lea Gardine, Kara Gately, Peter Haeussler, Wael Hassan, Franz Meyer, Cole Richards, Natalia Ruppert, Carl Tape, John Thornley, Rob Witter

The content of the main article spans a range of disciplines. Where possible, we have focused the article on summary observations. The purpose of this electronic supplement is to provide depth to many of the topics discussed. We do this by including: (i) methodological descriptions; (ii) a table with supporting details; and (iii) figures that illustrate various discussion points; and (iv) photographs that provide examples for some of the observations presented in the main article. While the main article was written to stand on its own, all of the content in this supplement is referenced from the article and will hopefully be of value to the motivated reader.

Supplemental Text

Text S1: Moment tensor methodology

We use long-period regional seismic waveforms and a modified version of the ‘cut-and-paste’ (CAP) code (Silwal and Tape, 2016; Zhu and Helmberger, 1996; Zhu and Ben-Zion, 2013) to estimate point-source moment tensor for mainshock. We calculate synthetic seismograms using the frequency-wavenumber approach (Zhu and Rivera, 2002) and the standard 1D model used in southern Alaska for earthquake location and moment tensor estimation. For the bandpass periods of 40–200 s, the waveforms can be well-modeled assuming a simple layered model of Earth structure and a point source representation for the earthquake. We generate a large number of uniformly distributed moment tensors, evaluate a waveform misfit function between recorded and synthetic seismograms, and then choose the moment tensor that provides the lowest misfit (i.e., best waveform fit). We perform two grid searches over the space of moment tensors and depths. In the first search, we constrain the moment tensor to be a double couple, which is equivalent to assuming that the earthquake ruptured on a single plane. In the second case, we search the full space of moment (FMT) tensors (e.g., Alvizuri and Tape, 2016; Alvizuri et al., 2018). For each case, after we establish the best-fitting depth, we perform an additional grid search using $\Delta M_w = 0.01$ to obtain a more precise magnitude estimate. As we would expect, the waveform fits are quantitatively better in the case where a larger parameter space is allowed (i.e., FMT). The FMT solution contains a small negative isotropic component; a more extensive analysis is needed to investigate whether this result is statistically significantly different from the best-fitting double couple. The choice of moment tensor constraint (DC, deviatoric, FMT) will impact other source parameters, notably depth and magnitude, but also the orientation. For example, in our case, constraining the moment tensor to be a DC changes the depth from 45.2 to 50.2 km (bracketing the first motion-derived hypocenter depth) and the magnitude from 7.07 to 7.09 (Richards, 2019, Table M1). The two possible fault planes are either east-dipping 30° or west-dipping 60°.

Text S2: SARVIEWS Data Processing

The SARVIEWS system features both amplitude and phase-based products to support situational awareness and enable tracking of an ongoing event (Figure S3). All processing is currently based on full-frame Sentinel-1 SLC products. A move to burst-based processing is currently being considered.

The workflows behind the main SARVIEWS hazard products are schematically shown in Figure S3. Phase-based (InSAR) products (Figure S3; top row) include wrapped image products to support situational awareness as well as unwrapped line-of-sight deformation maps and coherence maps for more quantitative analysis. A more detailed description of our fully-automatic InSAR workflows is published in (Meyer et al., 2015). Amplitude products (Figure S3; middle row) include fully terrain corrected and radiometrically corrected image time series products (Meyer et al., 2015) as well as change detection maps (Ajadi et al., 2016). RGB-colored image products utilize the polarization diversity available in the dual-pol Sentinel-1 data. They were developed to improve the interpretability of SAR images by analysts used to colorized optical data. The approach decomposes the co- and cross-pol signal into simple bounce (polarized) with some volume scattering, volume (depolarized) scattering, and simple bounce with very low volume scattering. These are assigned to the red, green and blue color channels, respectively (Figure S3; bottom row).

To reduce the need for user interaction, we fully automated the SARVIEWS production chains by integrating with the USGS earthquake and volcano notification services (ENS and VNS, resp.). A cron-job regularly checks for incoming hazard notifications. If a notification is detected that meets pre-defined event criteria, a SARVIEWS subscription is automatically created and production of InSAR and amplitude-based hazard products commences. For earthquake events, processing starts with the event date and continues for a period of three months to capture potential post-seismic deformation. All SARVIEWS products are being made available free-and-open to the general public via the SARVIEWS hazard portal (<http://sarviews-hazards.alaska.edu>).

SARVIEWS data processing continued until Feb 22, 2019, two months after the event. At the time of writing, a total of 18 co-seismic and 38 post-seismic interferograms were automatically processed and made available. All data products specific to this event can be downloaded from <http://sarviews-hazards.alaska.edu/Event/134>.

Supplemental Tables

Table S1.

National Tsunami Warning Center event chronology.

National Tsunami Warning Center Event Chronology: Nov. 30, 2018			
Time [UTC]	Minutes after O-time	Event	Additional Information
17:29	0:00	Large Local Earthquake	
17:32	0:03	Tsunami Information Statement #1	Issued for a Magnitude 7.0. Initial estimates showed good agreement for $M_w=6.8-7.0$. Below threshold ($M7.1$) for a local warning. However, around 5 minutes after o-time Earlybird software analysis was for $M_w=7.2-7.4$
17:35	0:06	Tsunami Warning #1	Magnitude 7.2, Tsunami Warning for Cook Inlet and the lower Kenai Peninsula following NTWC special procedures for interior waterways ($M \geq 7.1$)
17:54	0:25	$M_w 7.17$	Personal communication with Pacific Tsunami Warning Center
17:58	0:29	$M_w 7.0$	Personal communication with National Earthquake Information Center (NEIC)
18:00	0:31	Conference Call #1	Local warning. No danger for West Coast or other parts of Alaska. Concern not for faulting mechanism or the rupture causing a tsunami, but for localized effects causing coastal hazard from ground failures (landslides, slumping, liquefaction). No anomalous water level observations on the Anchorage tide gauge at this time. NTWC monitoring all tide gauges in Cook Inlet, and fully operational, but our observational network does not provide enough information to ensure all coastlines are safe immediately. NTWC will wait to issue an all clear and cancel the warning.
18:05	0:36	Tsunami Warning #2	Tsunami Warning continues
18:10	0:41	Ongoing decision support and analysis	AEC/USGS ShakeMap and Ground Failure Maps reviewed
18:24	0:55	$M_w 7.06$	Personal communication with Pacific Tsunami Warning Center
18:29	1:00	Tsunami Warning #3	Tsunami Warning continues
18:55	1:26	Conference Call #2	A sufficient amount of time has passed with no observations on any coastal tide gauges. No reports from any constituents of hazardous water or ground failure.
18:58	1:29	Cancellation	

Supplemental Figures

Figure S1. Tsunami alert levels defined. Credit: NOAA National Weather Service.





Tsunami Alerts		
Alert Name	Actions	Potential Hazards
 WARNING	Get to high ground or inland IMMEDIATELY Follow tsunami evacuation signage	DANGER! TSUNAMI IMMINENT! Flooding/powerful currents Wave heights > 3 ft. or unknown
 ADVISORY	Stay out of the water and away from the shore	STRONG CURRENTS AND DANGEROUS WAVES in or very near coastal water Wave heights of 1 - 3 ft.
 WATCH	Be prepared to take action Stay tuned to local radio/TV/ NOAA "alert" weather radios	TSUNAMI IS POSSIBLE Alert level may change once more information is known
 INFORMATION STATEMENT	No action needed	NO TSUNAMI IMPACT EXPECTED Alert level may change once more information is known
THREAT Message: Intended to alert international partners only. Not applicable to U.S. coasts		
THE NATIONAL TSUNAMI WARNING CENTER ISSUES OFFICIAL TSUNAMI ALERTS. CHECK TSUNAMI.GOV OR WEATHER.GOV WEBSITES FOR TSUNAMI ALERT DETAILS.		

Figure S2.

From the USGS Ground Failure overlay showing Liquefaction and Landslide potential.

<https://earthquake.usgs.gov/earthquakes/eventpage/ak20419010/ground-failure>

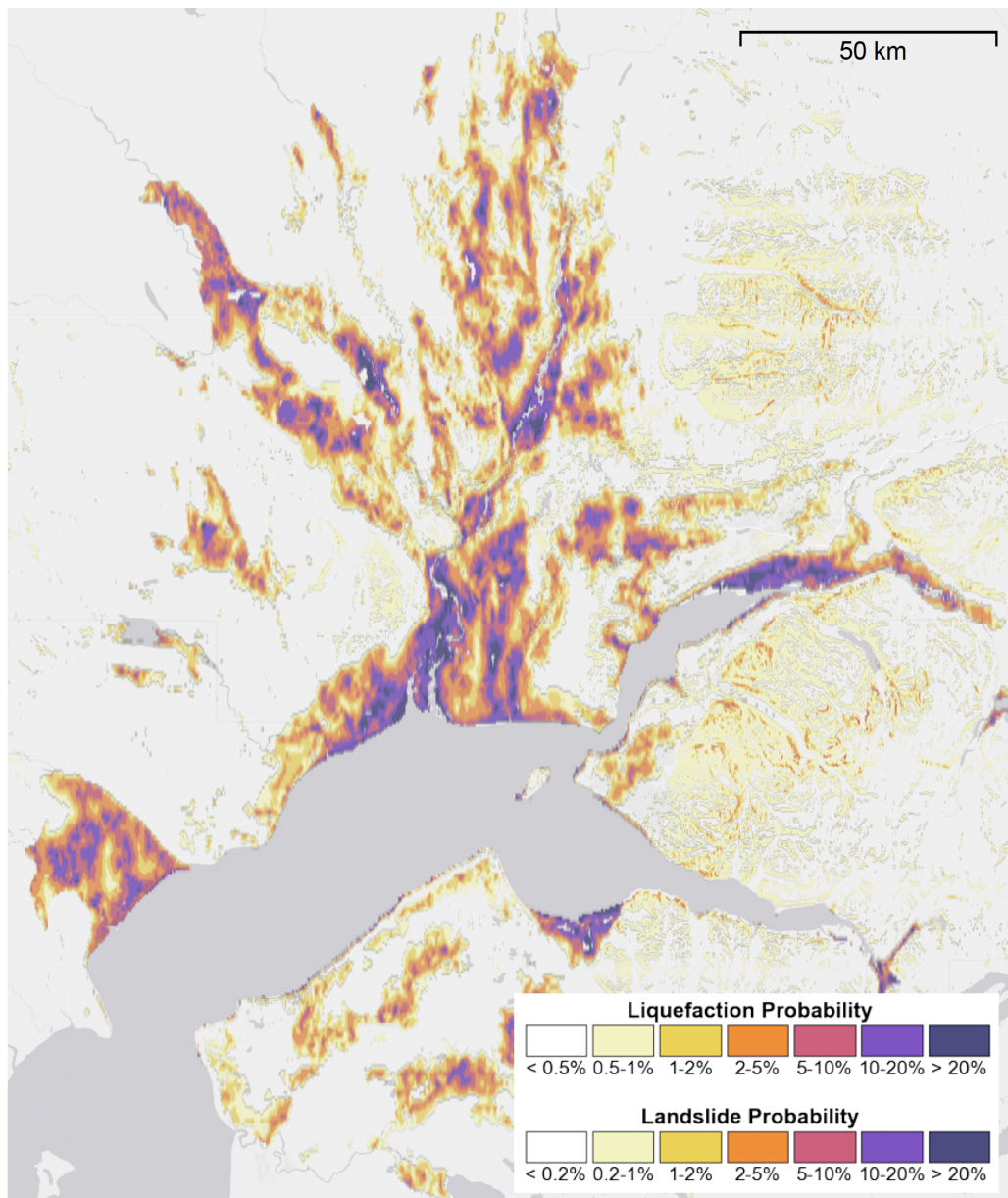


Figure S3.

SARVIEWS processing scheme for automated InSAR product delivery. See Meyer et al. (2015) for thorough treatment. <http://sarviews-hazards.alaska.edu>

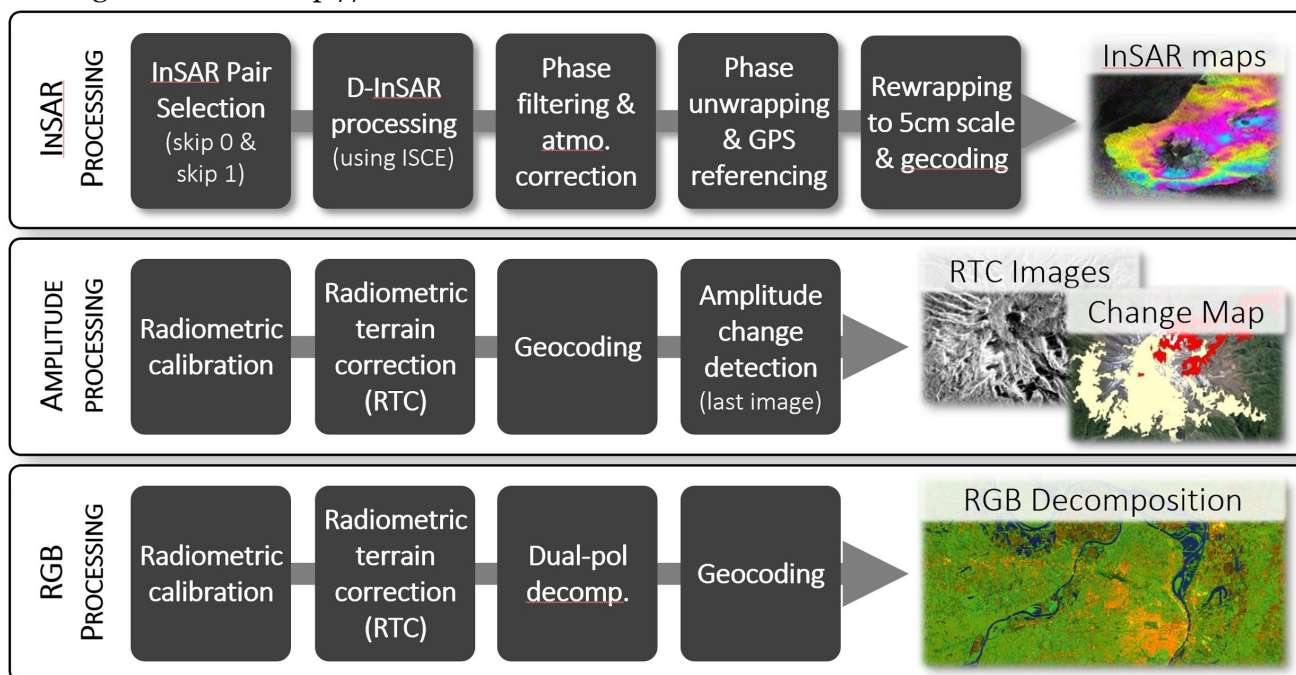


Figure S4.

Cross-section through aftershocks illustrating the approximate hypocentral distance to various communities. Cross-section cuts roughly perpendicular to the slab dip. Seismicity prior to 30 November 2018 marked in black. Mainshock and aftershocks are white.

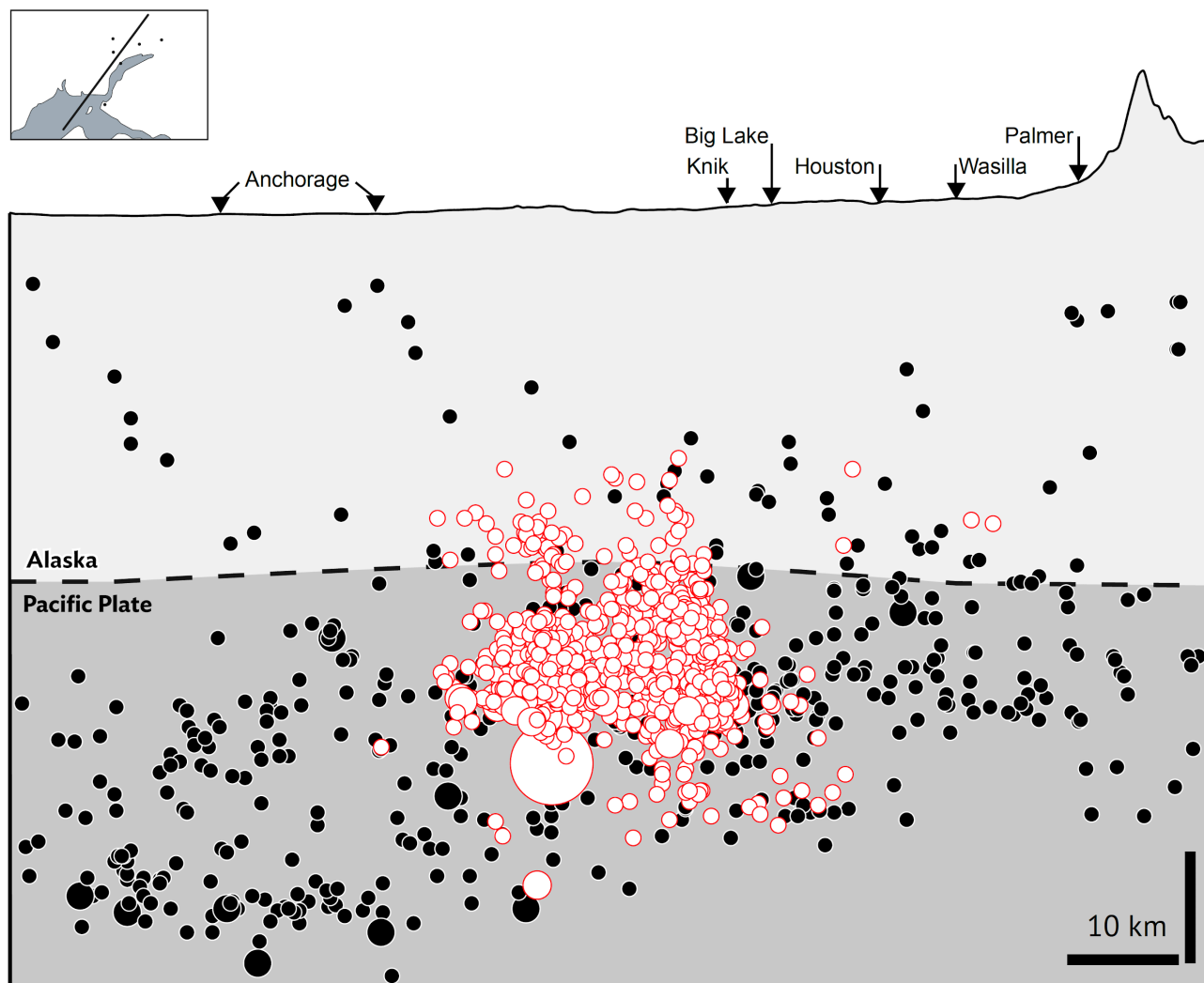


Figure S5.

Stream discharge as a potential function of deformation and ground motion. A. Log-log plot of absolute increase in discharge versus pre-earthquake discharge. B-D. Plots of percent increase in discharge versus: B. InSAR-derived line-of-sight displacement, C. PGA, and D. distance from mainshock hypocenter.

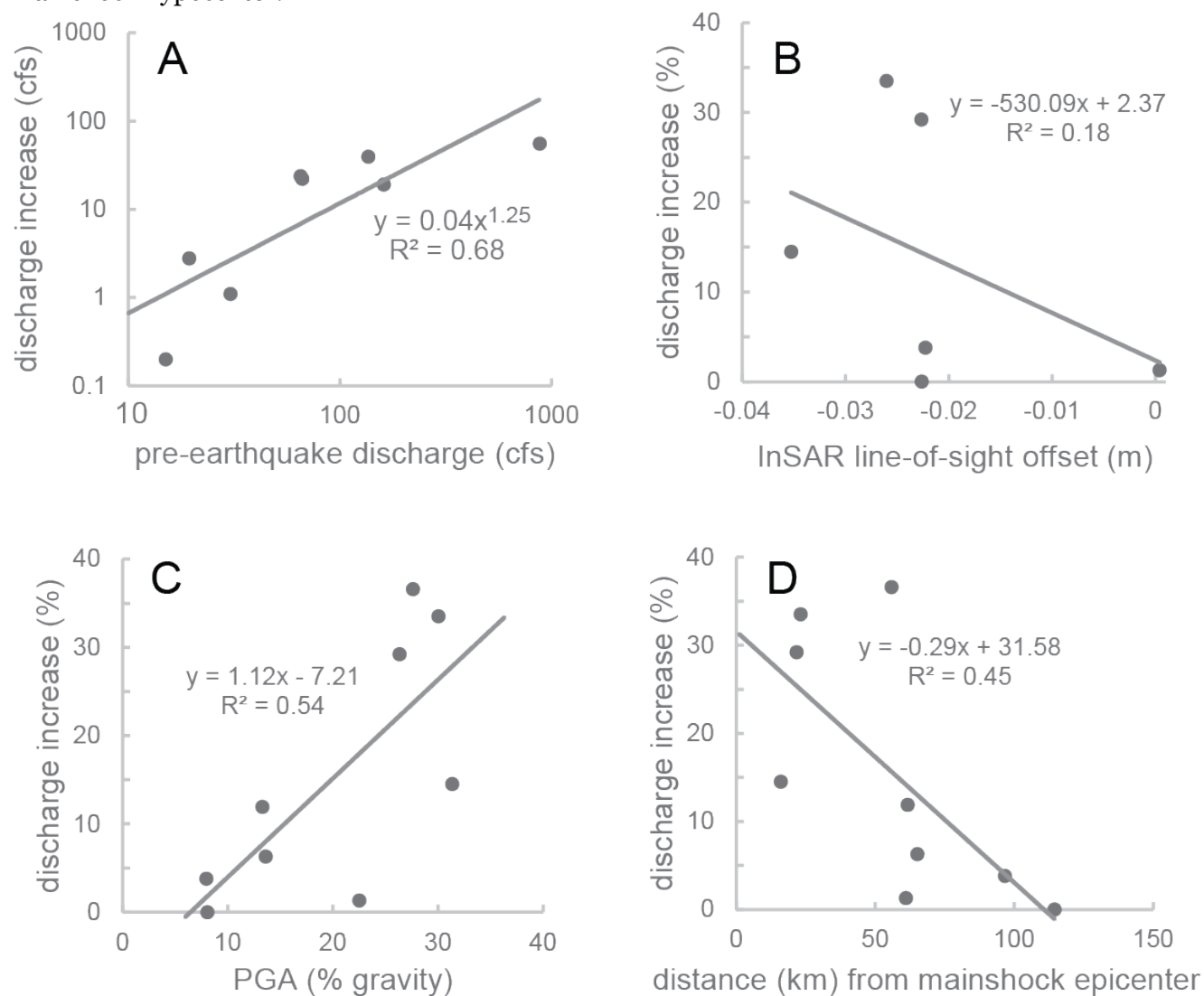


Figure S6.

Large rockfall on a southeast-facing slope of Rainbow Peak, about 13km miles east of Potter Marsh along the Seward Highway (61.0023° , -149.6453°). Within three to four days after the earthquake, newly fallen snow had obscured this landslide. Photo: Jeremiah Drage.



Figure S7.

Debris avalanches on steep canyon walls composed of glacial outwash sediments along the Eklutna River. View to the southeast (61.4202°, -149.2207°) Photo: Rob Witter



Figure S8.

Sediment vented by earthquake-triggered liquefaction at the mouth of the Little Susitna River. This view is looking south over Cook Inlet. (A) Extensive liquefaction shown by dark ejected sediment deposited on frozen ground. White spots may indicate sources of ejected material. (B) Lateral spreading and ejected liquified sediment. (C) White circular depressions interpreted as water frozen overnight in source vents of liquified sediment. (D) Lateral spreading, likely involving channel-parallel extensional ground cracking, and expulsion of fluidized sediment evident as black and brown deposits on snow. (61.2860°, -150.2980°) Photo: Rob Witter.



Figure S9.

Complex earthflow slumping along the Alaska Railroad southern line overlooking tidal flats along Knik Arm, near Mirror Lake in this view toward the south. Failure of these low bluffs may have involved liquefaction. (61.4376°, -149.4496°) Photo: Rob Witter.



Figure S10.

Lateral spreading disrupted Vine Road near the town of Wasilla in this view looking north. Many failures of engineered materials occurred on or adjacent to saturated lowlands filled with organic sediment, silt, or sand. (61.4376°, -149.4496°) Photo: Marc Lester.



Figure S11.

House built on anthropogenic fill. Significant ground cracks and settling are present. Variable settling is indicated well by the tilted rooflines and gap between the structures. The sloped driveway demonstrates how, in this neighborhood, a large volume of soil was used to elevate structures above street level. Settling in these types of soils was one of the primary drivers of residential damage. (61.1380°, -149.9379°) Photo: Michael West.



Figure S12.

House built partly on fill materials. The foundation of the house was compromised when soils settled and moved away from the structure. Photo: Loren Holmes.



Figure S13.

Comparison of building damage and ground motion in the vicinity of Eagle River and Chugiak, north of downtown Anchorage. (Left) Original inspection placard value. Source: Municipality of Anchorage Geographic Data and Information Center. Last retrieved: April 26, 2018. (Right) Observed PGA ground motions supplemented with PGA values inferred from DYFI reports.

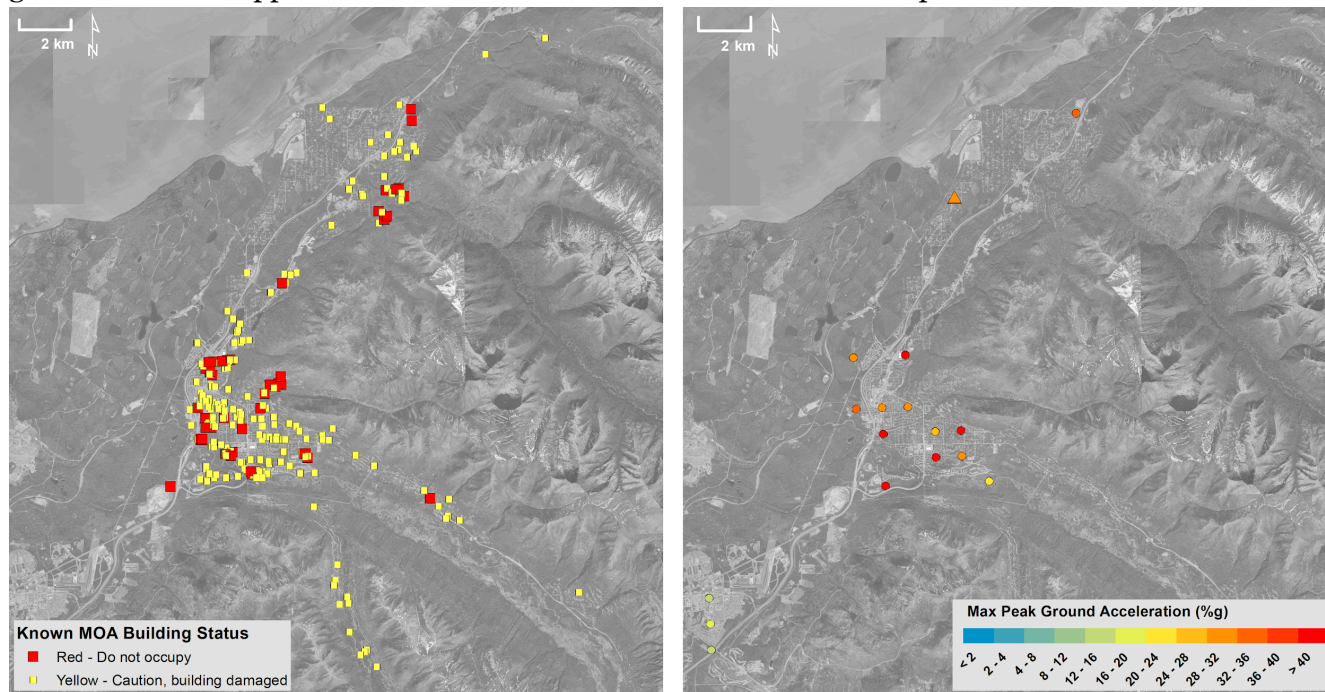


Figure S14.

Examples of damage in non-engineered single-family houses. (Left) Porch cover detached from house and fell in front of doorway. Photo: Wael Hassan. (Right) Substantial wall cracks. Photo: Chris Motter.

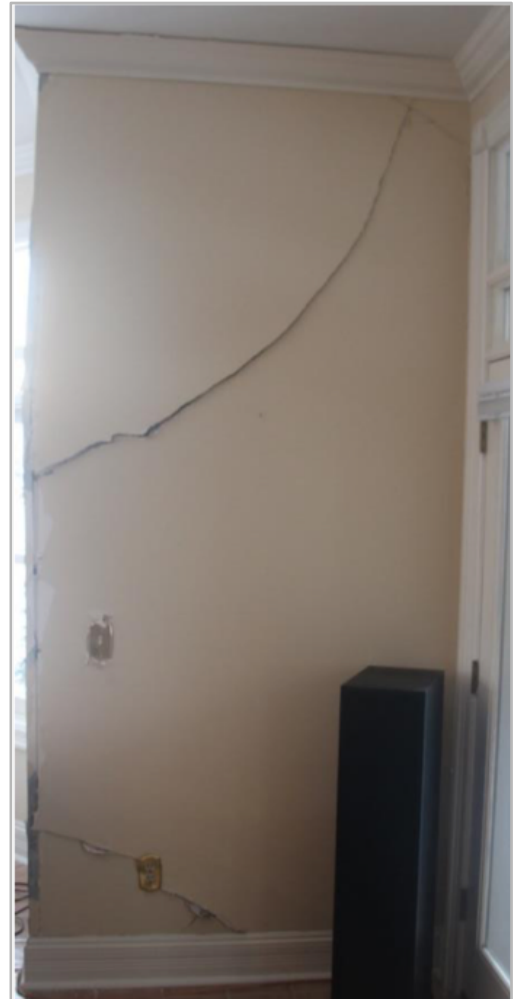


Figure S15.

Examples of CMU (concrete masonry unit, or “cinder block”) failures. (Top left) Shifting between blocks. Photo: Janise Rodgers. (Top Right) Buckled CMU wall temporarily buttressed for safety. Photo: Wael Hassan. (Bottom left) A failed CMU wall-to-floor joist connection at a school in the Mat-Su region. Photo: Bill Noyes. (Bottom right) Severe cracking and spalling in a CMU wall that exposed structural columns at a school gymnasium in the Mat-Su region. Photo: Wael Hassan.



Figure S16.

Examples of typical non-structural damage.

(Top) Suspended ceiling grids proved particularly susceptible to damage. Photo: Wael Hassan. (Middle) Pipe connections were sheared from unstrapped water boilers atop a 14-story Anchorage building causing several floors to flood. Photo: Wael Hassan. (Bottom) Failures in the fire suppression system—pipes and sprinkler heads—at the Alaska Airlines Center caused the arena to flood. Photo: University of Alaska Anchorage.



Figure S17.

Examples of school damage. (Top) Major non-structural ceiling damage in a classroom. Photo: Mat-Su School District. (Bottom) Major structural damage in an exterior brick wall at Eagle Elementary School. Photo: Chris Motter.



Figure S18.

Bridge damage. (Top) Major cracking in a bridge wall. Photo: Alaska Department of Transportation. (Bottom) Moderate to severe shear-key damage exposing the embedded steel reinforcement. Photo: Alaska Department of Transportation.



References

- Ajadi, O., F. J. Meyer, and P. W. Webley (2016). Change Detection in Synthetic Aperture Radar Images Using a Multiscale-Driven Approach, *Remote Sensing*, 8(6), 482, doi.org/10.3390/rs8060482
- Alvizuri, C., and C. Tape (2016). Full moment tensors for small events ($M_w < 3$) at Uturuncu volcano, Bolivia, *Geophys. J. Int.*, 206, 1761–1783, doi:10.1093/gji/ggw247.
- Alvizuri, C., V. Silwal, L. Krischer, and C. Tape (2018). Estimation of full moment tensors, including uncertainties, for nuclear explosions, volcanic events, and earthquakes, *J. Geophys. Res. Solid Earth*, 123, 5099–5119, doi:10.1029/2017JB015325.
- Meyer, F. J., McAlpin, D. B., Gong, W., Ajadi, O., Arko, S., Webley, P. W., & Dehn, J. (2015). Integrating SAR and derived products into operational volcano monitoring and decision support systems. *ISPRS J. Photogrammetry and Rem. Sensing*, 100, 106–117. <https://doi.org/10.1016/J.ISPRSJPRS.2014.05.009>.
- Richards, C. (2019). Moment tensors for the mainshock and aftershocks of the 2018-11-30 $M_w 7.1$ Anchorage earthquake. ScholarWorks@UA. <http://hdl.handle.net/11122/10173> (last accessed 2019-05-16).
- Silwal, V., and C. Tape (2016). Seismic moment tensors and estimated uncertainties in southern Alaska, *J. Geophys. Res. Solid Earth*, 121, 2772–2797, doi:10.1002/2015JB012588.
- Zhu, L., and Y. Ben-Zion (2013). Parameterization of general seismic potency and moment tensors for source inversion of seismic waveform data, *Geophys. J. Int.*, 194, 839–843, doi:10.1093/gji/ggt137.
- Zhu, L., and D. Helmberger (1996). Advancement in source estimation techniques using broad-band regional seismograms, *Bull. Seismol. Soc. Am.*, 86(5), 1634–1641.
- Zhu, L., and L. A. Rivera (2002). A note on the dynamic and static displacements from a point source in multilayered media, *Geophys. J. Int.*, 148, 619–627, doi:10.1046/j.1365-246X.2002.01610.x.